International Journal for Numerical and Analytical Methods in Geomechanics

WILEY

RESEARCH ARTICLE OPEN ACCESS

Bearing Capacity of Tension Steel Piles in Thinly Inter-Layered Soils: Numerical Class-A Prediction vs. Field Measurements

Diaa Alkateeb | Jürgen Grabe

Institute of Geotechnical Engineering and Construction Management, Hamburg University of Technology (TUHH), Hamburg, Germany

Correspondence: Diaa Alkateeb (diaa.alkateeb@tuhh.de)

Received: 4 July 2024 | **Revised:** 16 May 2025 | **Accepted:** 6 August 2025

Keywords: fibre-optic measurements | finite element prediction | inter-layered soils | pile–soil interaction | pull-out resistance

ABSTRACT

This study investigates the bearing capacity of tension piles and pile-soil interaction during loading. Discrepancies between predicted and measured bearing capacities in previous tests motivated the study, where analytical methods showed considerable scatter and uncertainties in design. A large-scale field test was conducted on three additional adjacent tension piles (Pile 1, 2 and 3), featuring extensive fibre-optic strain measurements. Concurrently, a numerical Class-A prediction was developed beforehand to analyse pile-soil interaction and predict bearing capacity, utilising hypoplastic and visco-hypoplastic models for the thinly inter-layered subsoils. The fibre-optic measurements revealed significant locked-in bending strains post-installation, prior to loading. The results showed a correlation between pronounced bending strains and lower load-bearing capacity. Numerical predictions were compared with the field measurements, providing good agreement with Pile 1, which exhibited minimal installation-induced bending and thus represented an idealised case. This comparison offered valuable insights into tension pile failure mechanisms and load capacity. This research enhances understanding of tension pile behaviour in complex soils and underscores the necessity of optimising installation methods to improve load-bearing capacities.

1 | Introduction

In geotechnical engineering, tension piles are often used to transfer loads to deeper, load-bearing soil layers. They also serve as anchors. Compared to conventional anchors, tension piles are characterised by simpler and more cost-effective production, higher resistance to lateral loads, and the capacity to bear compressive forces. To reinforce the bank walls of the lower harbour for the new Niederfinow ship lift in Germany, driven steel piles of the HP 320 × 88.5 type were selected due to their advantages. Estimating the characteristic pile shaft resistance was based on empirical values recommended by EA Pfähle [1], which necessitates conducting pile load tests on tension piles besides relying on empirical values. In 2017, six vertical test loads were conducted at three different locations, as seen in Figure 1 in blue, to determine the pull-out bearing capacity. However, the measured resistance during the pile test loading fell significantly below the predicted values, ranging from only 22 % to 49 % of the planned test loads. A new fourth load test program was implemented to investigate the factors causing this low load-bearing capacity of the driven steel piles. This large-scale field test involved three adjacent piles of the same type, seen in Figure 1 in red. This new test program featured enhanced instrumentation, notably high-resolution fibre-optic measurements, specifically aimed at investigating the mechanisms behind the unexpectedly low capacities observed in the earlier, standard verification

https://doi.org/10.1002/nag.70132

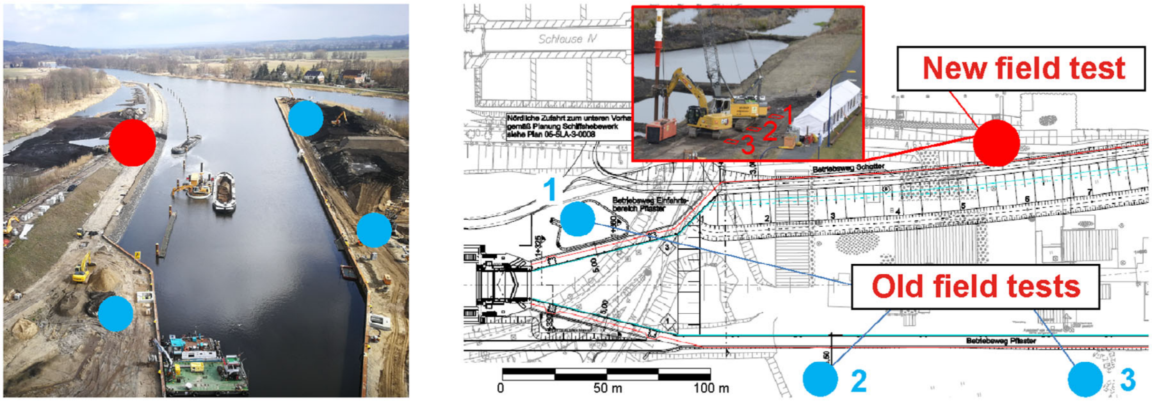

FIGURE 1 | Site plan of the Niederfinow ship lift showing test pile locations: aerial view (left) and map view (right). Blue dots indicate the locations of previous pile load tests (sites 1–3), while the red dot marks the location of the new field tests, indicating three adjacent piles tested at the new site to investigate the reduced load-bearing capacity observed in earlier tests.

pile tests. Throughout the test loading of the piles, extensive measurements were carried out on the piles and the surrounding soil.

Simple (analytical) methods are commonly employed to determine the maximum tension-bearing capacity of pile foundations. However, the limitations of these methods arise due to their simplistic assumptions, which overlook the complex nature of soil behaviour and pile-soil interactions. These limitations result in significant uncertainties and discrepancies between theoretical calculations and actual measurements.

This paper provides an overview of analytical methods and their limitations. It presents a large-scale field test accompanied by a numerical Class-A prediction to investigate the ultimate pull-out bearing capacity of tension piles in thinly inter-layered soils and evaluate the pile-soil interaction during loading. It is worth noting that the investigation of piles in thinly inter-layered soils, to the authors' knowledge, is an area that has rarely been explored in the existing literature. The measurement program employed in this study went beyond the standard pile load test setup, incorporating fibre-optic measurements within the steel piles. This approach allows for the identification and evaluation of the strain distribution across the depth of the pile, facilitating the consideration of load-bearing and non-load-bearing layers.

The Class-A prediction also aims to provide insights into the failure mechanism of the piles under vertical loading. Predictions are a crucial aspect of geotechnical engineering. While predictions can be made intuitively or empirically, numerical predictions using mathematical models are now expected [2]. Lambe [3] categorises predictions in geotechnical engineering into three classes based on their timing. Class-C predictions are made after an event, Class-B during, and Class-A before an event. Lambe [3] also laid out the framework for geotechnical prediction. The process comprises six steps: determining and simplifying the field situation, identifying the system's mechanisms, selecting suitable methods and parameters, conducting the prediction, and finally, comparing it with field test data. While there are many publications on Class-C predictions, Class-A predictions are rare [2]. Class-A predictions are better suited for testing new simulation methods. However, they may result in significant discrepancies between calculation and observation, as they rely solely on information available at the time of prediction. The accuracy of predictions is limited by difficulties in determining exact field situations, relevant mechanisms, and soil properties.

2 | Bearing Capacity of Driven Steel Piles

The load-bearing capacity of tension piles is determined by mobilised skin friction Q_s. In contrast to a compression pile, there is no base resistance Q_b, which could contribute to the total resistance Q_c. The load-displacement curve of a tension pile accordingly shows a mobilisation of the maximum resistance already at minimal displacements. After reaching the limit state, resistance typically does not increase further. The skin friction force results from the shear stress q_s on the skin surface A_s:

$$Q_{c(\text{tens})} = Q_s = q_s \cdot A_s \tag{1}$$

2.1 | Analytical Methods to Determine the Maximum Bearing Capacity

Various published 'analytical'approaches can be categorised into three main groups for calculating the ultimate tensile strength of tension piles (for brevity, these are commonly referred to as analytical methods, although some are empirical or semi-empirical in nature). The first group consists of values derived purely from empirical observations [4]. The second group relies on Coulomb's shear law as its foundation [5]. The third group assumes activation of a soil body surrounding the pile in the ultimate limit state [6]. These methods are typically chosen due to their practicality and simplicity. Various standardised calculation methods are utilised to assess the tensile load capacity of piles based on prior load tests at sites 1, 2, 3 and the newly added site 4, see Figure 1. The input parameters for the soil layers are derived from cone penetration test (CPT) data, following the guidelines outlined in CPT-Guide [7], and are presented in Table A1 in Appendix A. The input parameters are also documented in [8]. The testing procedures were consistent across all sites and are detailed with the soil conditions in Section 3. The methods employed in this study to calculate the maximum

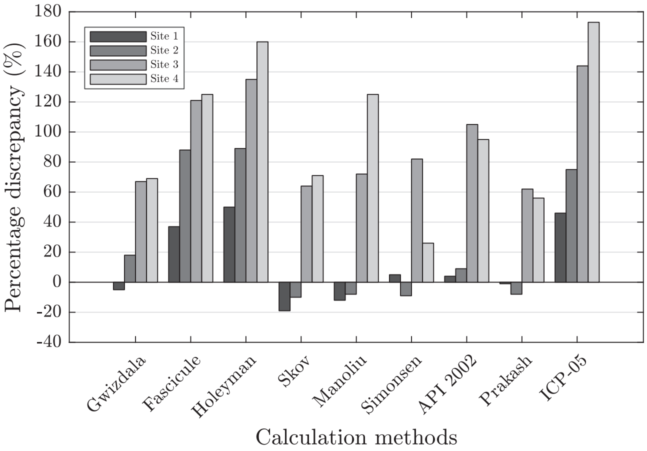

FIGURE 2 | Percentage discrepancy between analytically calculated and experimentally measured ultimate bearing capacities across four test sites, comparing nine established calculation methods. Positive values indicate overestimation of bearing capacity by the analytical method, while negative values represent underestimation.

bearing capacity draw upon a range of sources. Some methods, as per their authors, apply to multi-layered soils with H-shaped steel profiles without limitations, such as [9, 10], and the ICP-05 method [5]. In contrast, others are restricted to round piles or monopiles, like [11–16]. Detailed formulas and calculation procedures for each method can be found in their respective publications. The calculated capacities are compared to the averaged actual measured capacities of the piles at each site.

Figure 2 graphically represents the discrepancies between calculated and actual measured values from the load tests. Positive deviations indicate overestimations, while negative values highlight underestimations. Notably, all methods show a considerable variance in estimations, with some methods at specific sites resulting in over 140 % overestimation, while others underestimate capacities by nearly 20 %. The analysis across different computational methods indicates uncertainties in the design of tension piles. Furthermore, the results emphasise the pressing need for further research on tension steel piles, especially in soils with alternating thin layers.

Conventional analytical models have evident limitations: they often overlook complexities in soil behaviour and pile installation effects, and they oversimplify layer distribution and pile type. This leads to discrepancies between theoretical predictions and field measurements. Factors such as stress relaxation, creep, ageing, soil displacement into the underlying layer and chemically induced changes in the friction angle at the pile-soil interface are frequently neglected, along with the effects of pile installation. These oversights contribute to the considerable variability and uncertainty observed in analytical design methods. Moreover, field studies indicate a significant difference in skin friction between compression and tension piles, with friction ratios ranging from 0.44 to 0.9 [17–19]. Some design guidelines, therefore, recommend a reduction factor of 10 to 30 % for tensile loads, such as in the API guidelines [16]. This discrepancy arises from changes in effective stress levels and reduction in the diameter of piles under tension [18]. Additionally, tension piles may undergo stress direction rotation, affecting their effective stress levels [20]. These insights highlight the critical need for incorporating differential skin friction considerations as well as installation effects into pile design, an aspect often overlooked in some current practices, underscoring the limitations of existing analytical methods.

2.2 | Literature Review on Thinly Inter-Layered Soils

To our knowledge, no published research exists on tension pile behaviour in inter-layered soils. In contrast, numerous studies have explored Cone Penetration Testing (CPT) in such soils, although many typically focus on simpler two- or three-layer systems. For example, in a study by van der Linden [21], model tests involved soils with multiple alternating layers of sand and clay within a cylindrical container. These tests showed differences in behaviour between 20 and 80 mm-thick clay and sand layers. In the latter, peak resistance did not match a reference sand's resistance. The deviation with the 20 mm layers was even more pronounced. The contrast in the cone resistance between the clay and sand layers was also less distinct. All tests revealed that pore water pressure increased within the clay layer only after the probe advanced a certain distance. The authors speculated that sand was pushed into the clay ahead of the probe. The spreading of clay into sand has also been observed by others, for example, with sheet piles like in [22] and with piles in [23]. Another study by de Lange [24] conducted similar tests but could not distinguish between individual sand and clay layers at low thicknesses in CPT results. Peak resistances in multi-layered systems are influenced by layer thickness, the number of layers in the zone of influence, and the characteristic resistances of individual layers. However, it is essential to note that the tested multi-layer samples had equal, homogeneous sand and clay layer thicknesses, which may not represent field conditions. The results underscore the complexity, especially when dealing with numerous very thin layers.

In a related study on the buckling analysis of piles in multi-layered soils [25], emphasised the susceptibility of piles to buckling in the presence of soft soil layers, contrasting significantly with behaviour in sand layers. This research highlights that buckling risks are heightened in soil profiles featuring soft layers or voids interposed between stiffer layers. Ofner [26] similarly underscored that soft soil layers significantly affect micropiles' buckling resistance, particularly in terms of load transfer through skin friction and lateral support. This insight contributes to understanding pile behaviour in complex soil conditions, aligning with observations in multi-layered soil systems where thin layer distinctions pose challenges for predicting pile and probe responses.

3 | New Field Test in Niederfinow

The measurement site is situated on the northern bank of the lower outer harbour at the new ship lift in Niederfinow, located about 60 km northeast of Berlin. The three piles of the HP 320 × 88.5 type were installed using a combined installation method: the initial 6 m were installed via vibratory driving, followed by impact driving for the remaining 12.3 m to achieve the total installation depth of 18.3 m. This procedure was used

TABLE 1 | Geometrical and mechanical properties of the HP 320 × 88.5 steel pile profile with corresponding cross-sectional dimensions shown in the schematic.

Steel profile	HP 320 × 88.5
Steel grade	S355
Density ρ	7.87 t/m^3
Young's Modulus E	$210 \cdot 10^6$ kN/m^2
Poisson's ratio ν	0.3
Profile height h	303 mm
Profile Width b	304 mm
Flange width t_f	12 mm
Web width t_w	12 mm
Cross-section A	11,270 mm^2
Moment of inertia I	56,340,000 mm^4

to make the installation of the piles feasible, as the pile would exhibit substantial oscillation at the pile top if the pile were solely impact-driven from the first metre. In addition, the literature recommends vibrating the piles up to a few metres above the final depth and then impact-driving them for the last few metres [27, 28]. Technical Standards and Commentaries for Port and Harbour Facilities in Japan [29] also recommends conducting the last stage of the vibratory driving process through impact driving to enhance the pile's base resistance. Five weeks later, the piles were subjected to a test load and pulled out. Extensive measurements accompanied the pile load tests, incorporating fibre-optic strain measurements. The individual piles were spaced 8 m apart. Before installation, a borehole (BH) and a cone penetration test (CPT) were conducted near the central pile to determine the subsoil conditions. To ensure the verticality of the piles during installation, a pile driving guide, attached to an excavator, was employed to stabilise and guide each pile. The pile's properties and dimensions can be seen in Table 1.

3.1 | Fibre-Optic Strain Measurements

During the pile load testing, high-resolution fibre-optic strain measurements were conducted using two fibre-optic sensing cables (optical fibres) attached to the outer surface of a pile flange. This setup enabled detailed strain analysis during the subsequent test load. To install the fibre-optic sensing cables, grooves were initially created on the pile flange's outer side, as shown in Figure 3. The fibres were then placed in these grooves and affixed to the pile using a strong adhesive, illustrated in Figure 3. For these measurements, the LUNA OBR 4600 measurement system was utilised alongside Solifos FIMT CST-0.86/0.56 sensor cables, as provided by the company SENSICAL, which was also responsible for applying the fibre-optic measuring equipment and evaluating the strain data. The measurement principle is based on the coherent optical frequency domain reflectometry (c-OFDR) technique [30–32]. This technology allows for strain determination with a measuring point distance of 1 cm over a length of up to 70 m, resulting in a quasi-continuous strain curve along the pile. The technique measures the fibre's refractive index changes due to strain-induced elongation or compression. This deformation causes changes in the fibre's optical properties, such as phase shift or wavelength shift, which can be precisely measured and correlated to the applied strain. Transforming the measured signal into the frequency domain allows for direct determination of local strain based on the shift in frequency components, as illustrated in Figure 4. The relationship represented by Equation (2) applies to calculate the spectral shift ($\Delta\lambda$), where ε represents mechanical strain, ΔT is the temperature change, and K_ε and K_T are the strain and temperature constants of the fibre material, respectively.

$$\Delta\lambda = K_\varepsilon \cdot \varepsilon + K_\mathrm{T} \cdot \Delta T \tag{2}$$

The calibration of the fibre-optic sensors was conducted in a controlled laboratory environment using a specialised calibration setup. The sensors were subjected to various load cycles, ensuring the strain did not exceed 1 % to prevent any damage to the fibres. The spectral shifts recorded by the sensors under these conditions were then compared with precise strain measurements obtained from the calibration system. In our case, the temperature sensitivity of the fibre is not a significant concern because the fibre sensor was vertically embedded in the soil, where temperature conditions are nearly constant throughout the pile testing period. In the field test, the attached fibre-optic sensors underwent testing for integrity while the piles were horizontally supported at regular intervals by metal blocking, ensuring no bending occurred between the supports.

To safeguard the integrity of the fibres, no measurements were taken prior to or during the penetration phase of the piles. The risk of damaging the delicate glass fibres, particularly where the glued area ends at the pile top, was deemed too high due to the extreme stresses encountered during pile driving. The impact process, often involving significant forces from the hydraulic hammer and potential impacts with gravel or stones, could easily result in the breakage of the fibre cables. The impact forces during our tests damaged our instrumented accelerometers on the pile head, highlighting the extreme conditions the fibres and their connectors at the top of the pile would need to withstand if measurements were taken during this phase.

During the pile load testing, the measurements for each load stage were referenced against a pre-load or reference measurement conducted beforehand. The resulting changes in pile strain were derived from the spectral shift and plotted for all piles in microstrain units ($1\ \mu\varepsilon = 10^{-6}$ m/m) against the depth below the ground surface. Within each load stage, measurements were taken at the beginning and end of the stage. If the load was maintained for an extended period, intermediate measurements were generally conducted every 30 min.

3.2 | Static Pile Load Testing

The measurement concept and loading process for the test loads presented in Figure 5 followed a force-controlled approach, which will be shown later in the results discussion, involving incremental load increases while maintaining a constant tensile load within each load stage and measuring the resulting deformations. A hydraulic system was utilised to generate the load, capable of applying a maximum load of 3 MN with a maximum press

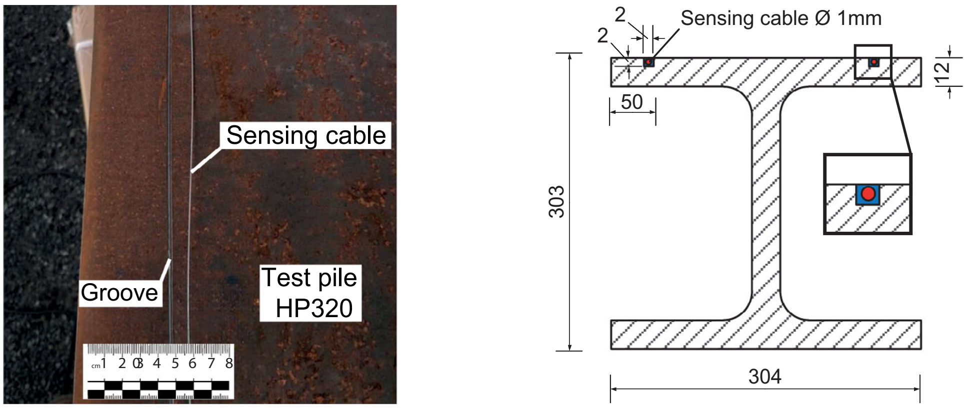

FIGURE 3 | Steel pile prior to instrumentation, displaying the embedded fibre-optic sensing cable within a milled groove (left) and cross-sectional view of the steel pile illustrating the positions of sensor cables with corresponding dimensions in millimetres (right).

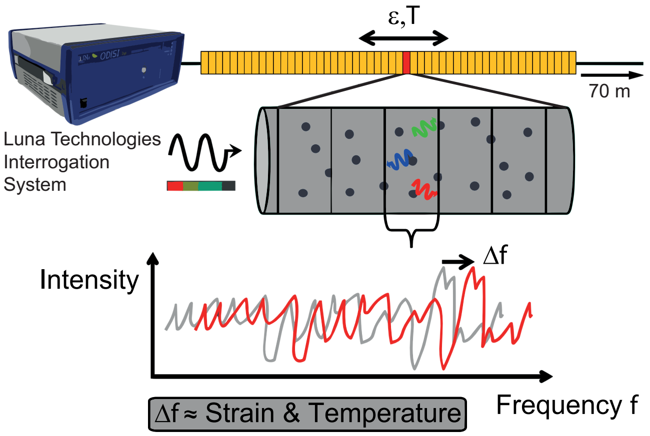

FIGURE 4 | Segmenting the strain signal of the measuring fibre into evaluation windows (top). Determination of the strain from the shift of the local frequency spectrum (bottom), quoted from [33].

stroke of 200 mm. The force was measured using a calibrated load cell positioned directly beneath the press. The test pile's vertical displacement was monitored using electrical precision dial gauges with a 0.01 mm resolution at four measuring points. The load steps were kept constant for at least 20 min, or until the displacement creep rate $K_s = 0.1$ mm in 5 min under constant load was reached. The test piles were initially loaded gradually in a first cycle, reaching the characteristic service load of 400 kN and then unloaded and reloaded until the respective test load, denoted as $P_P = 600$ kN, was achieved. The criteria for test failure were defined as either a displacement of 10 % of an equivalent circle diameter of the pile D_{eq}, a displacement creep rate of 2 mm per logarithmic time cycle, or the attainment of the designated test load P_P.

Key field implementation considerations for the new test program, beyond standard practices for the test layout, revolved around ensuring the integrity of the fibre-optic sensors post-installation and maintaining pile verticality. Mitigation strategies for these aspects, such as sensor protection and the use of a driving guide, are detailed within this section and Section 3.1. Data accuracy and reliability were ensured through several Quality assurance (QA) and quality control (QC) measures. These included pre-test calibration of all key instruments, employing redundancy in critical measurements (e. g., multiple dial gauges and fibre-optic lines per pile), and diligent inspection of collected data. Cross-validation of fibre-optic data against load cell readings, confirming its reliability, is presented in Section 6.

3.3 | Subsoil Conditions

The soil layers in the test area were identified through classification of the drilling log and laboratory testing of soil samples obtained from the borehole. The ground was simplified to nine representative layers: a layer of filling materials extending to a depth of 1.55 m, followed by a layer of peat spanning from 1.55 to 6 m in depth, and subsequently, uniform fine and coarse sand layers until reaching a depth of 12 m. Moreover, the soil profile exhibited multiple thin, alternating layers of fine sand and silt extending down to 17.3 m. Coarse-grained sand was found from a depth of 17.30 m below the ground surface, extending to the bottom of the drilled hole. Figure 6 shows the soil profile along with the tip resistance q_c and shaft friction f_s with depth. Furthermore, sand samples were collected from each representative layer in the borehole and classified using sieve analysis, identifying three main types of sand referred to as Sand I, II and III. The mean particle size distribution results are shown in Figure 7. Undisturbed peat and silt samples were collected from depths of 3.7 and 13.38 m respectively. For the cohesive layers, the void ratios were determined by the undisturbed collected samples. On the other hand, the void ratios and thus the relative densities of the non-cohesive layers I_D were derived from the cone penetration testing data (CPT) using Equation (3) according to Kulhaway [34]. q_c denotes the cone penetration resistance, p_a the reference pressure of 100 kPa and σ'_v the effective vertical stress. The void ratios can be determined from the relative densities using Equation (4) and were averaged within every layer.

$$I_D{}^2 = \frac{Q_{cn}}{350} = \frac{(q_c/p_a)/(\sigma'_v/p_a)^{0.5}}{350} \tag{3}$$

$$I_D = \frac{e_{max} - e}{e_{max} - e_{min}} \tag{4}$$

Table 2 summarise the properties of the Representative soil layers, featuring the mean grain size d_{50}, the coefficient of

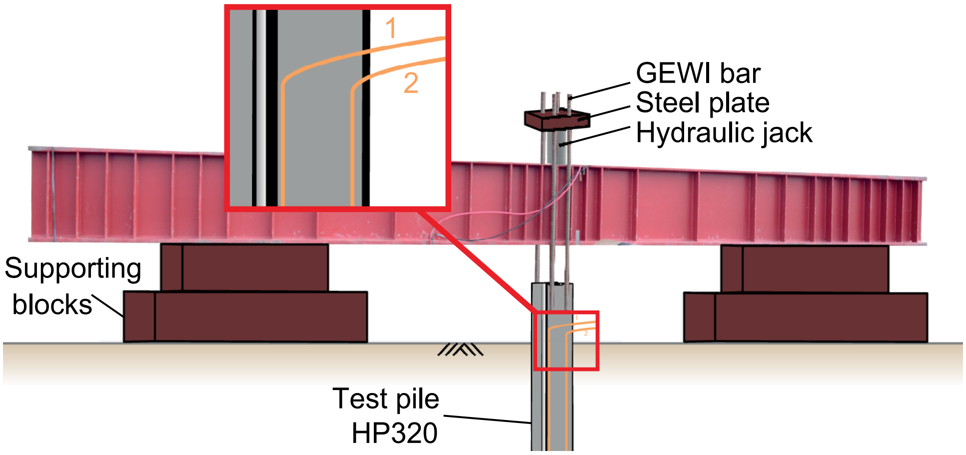

FIGURE 5 | Principal sketch showing the arrangement of the measuring instruments on the pile during the pile load test.

TABLE 2 | Characteristics and mechanical properties of the soil layers.

Layer No.	Depth (m)	Representative soil	d_{50} (mm)	C_u (-)	q_c (MPa)	e (-)
1	> 1.55	Sand II	0.23	2.3	8.0	0.67
2	1.55 to 6	Peat	—	—	0.5	2.72
3	6 to 8.8	Sand II	0.22	2.3	8.0	0.60
4	8.8 to 10	Sand III	0.33	2.7	25.0	0.45
5	10 to 12	Sand II	0.18	2.0	26.0	0.59
6	12 to 14.77	Silt/Sand I	—	—	3.0	0.51
7	14.77 to 16.43	Sand I	0.08	2.9	10.0	0.70
8	16.43 to 17.30	Silt/Sand I	—	—	3.0	0.70
9	< 17.30	Sand II	0.22	1.7	28.0	0.57

uniformity C_u, the average CPT resistance in field q_c and the void ratios e.

4 | Material Models and Parameter Calibration

An extensive laboratory testing program was conducted to determine and calibrate the soil's material parameters to ensure an accurate reflection of the physical properties and behaviours of the soil. Several laboratory tests were carried out focusing on different aspects of soil behaviour under various conditions, such as Consolidated Drained triaxial (CD), Consolidated Undrained triaxial (CU), Constant Rate of Load oedometer (CRL), and Constant Rate of Strain oedometer (CRS) tests. In addition, the void ratios were also calibrated in a numerical model of CPT testing to ensure that the numerical model could reliably simulate the soil's response in the pile load tests. The following sections detail the simulation's constitutive models and the calibration process for their parameters to achieve the optimal set of parameters.

4.1 | The Hypoplastic Model

The hypoplastic constitutive model according to von Wolffersdorff [35], including the intergranular strain extension according to Niemunis [36], was used for the simulations of the non-cohesive sands. This model realistically captures the non-linear and anelastic characteristics of granular materials, considering essential properties like dilatancy, contractancy, different loading and unloading stiffness, and the dependence of stiffness and strength on pressure and void ratio. For detailed information on the constitutive equations of the hypoplastic model with intergranular strain extension, please refer to Appendix B. The hypoplastic parameters were determined as follows:

- The critical friction angle φ_c is determined from the cone deposition test.
- The parameters h_s, n and β are determined from CRS oedometer.
- The minimum and maximum void ratios were assessed using standard tests. According to Niemunis [36], $e_{c0} = e_{max}$, $e_{d0} = e_{min}$, and $e_{i0} = 1.15 \cdot e_{max}$.
- The Exponent α depends on the relative density and the peak friction angle from a CD triaxial test.
- The five parameters of the intergranular strain m_R, m_T, R_{max}, β_R and χ are determined from a CD triaxial test with reversal of direction in the effective stress paths according to [37].

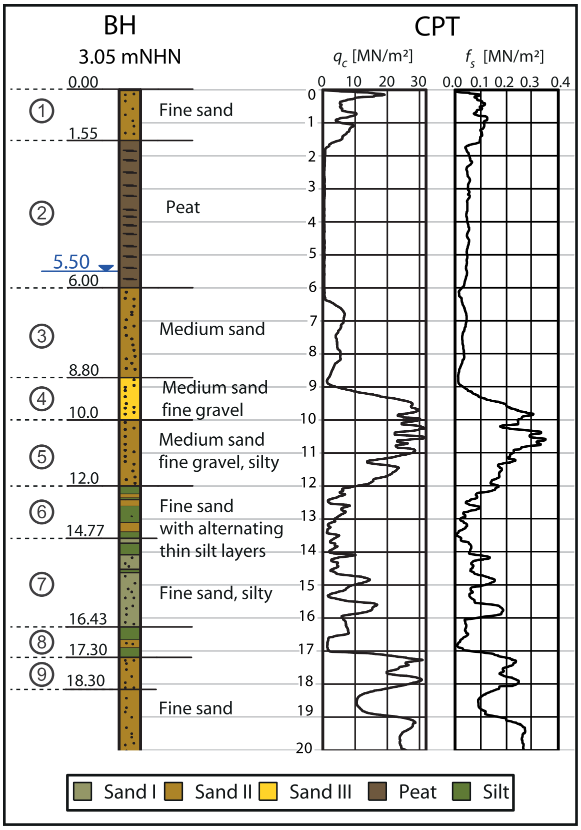

FIGURE 6 | The soil profile along with CPT sounding results at the site of the new pile load tests.

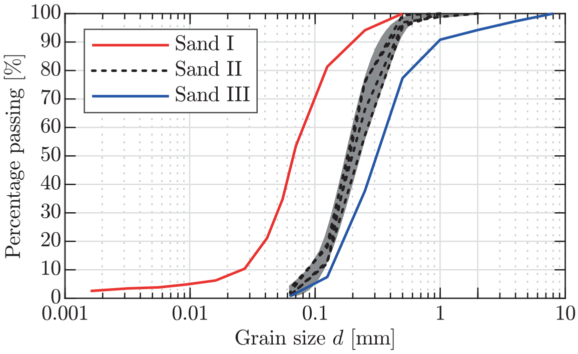

FIGURE 7 | Representative particle size distribution curves of the investigated sands (dashed curves resemble Sand II).

For clarity, only the results of the back-calculations for CD triaxial tests for various densities and stresses with the hypoplastic material model for non-cohesive sands are shown in Figure 8. Dashed lines depict the experiments, whereas solid lines represent the simulations. Overall, a good agreement between the simulations and the measurements is displayed. Table 3 shows the determined parameter sets of the hypoplastic material model for the three non-cohesive sands.

4.2 | The Visco-Hypoplastic Model

Cohesive soils were modelled using the visco-hypoplastic constitutive model by Niemunis [37]. This model, a development of the hypoplastic model, accurately accounts for fine-grained soil properties such as creep, relaxation, and rate dependence. According to Niemunis [37], the visco-hypoplastic model employs a rate-type equation, which is presented as follows:

TABLE 3 | Hypoplastic parameters for the investigated non-cohesive sands.

Parameter	Unit	Sand I	Sand II	Sand III
φ_c	(°)	32.85	31.24	30.18
h_s	(MPa)	1650	2442	2267
n	(-)	0.35	0.255	0.29
e_{d0}	(-)	0.48	0.47	0.37
e_{c0}	(-)	0.98	0.84	0.72
e_{i0}	(-)	1.12	0.97	0.83
α	(-)	0.055	0.09	0.15
β	(-)	1.56	1.65	1.3
m_T	(-)	1.46	1.53	1.17
m_R	(-)	4.68	4.52	4.65
R_{max}	(-)	$2.1 \cdot 10^{-4}$	$6.7 \cdot 10^{-4}$	$2.3 \cdot 10^{-4}$
β_R	(-)	0.16	0.58	0.8
χ	(-)	3.46	4.92	3.06

$$\dot{\boldsymbol{\sigma}} = \mathsf{L} : (\dot{\boldsymbol{\varepsilon}} - \dot{\boldsymbol{\varepsilon}}^{vis}) \, , \tag{5}$$

where L represents the linear part of the hypoplastic stiffness matrix and $\dot{\boldsymbol{\varepsilon}}^{vis}$ the viscous strain rate tensor. The intensity of the viscous strain rate tensor $\dot{\boldsymbol{\varepsilon}}^{vis}$ is governed by Norton's power law [38]. $\dot{\boldsymbol{\varepsilon}}^{vis}$ is given by Equation (6) and incorporates the flow rule $\mathbf{m}$:

$$\dot{\boldsymbol{\varepsilon}}^{vis} = D_r \left(\frac{1}{\mathrm{OCR}} \right)^{\frac{1}{I_v}} \mathbf{m} \, , \tag{6}$$

where D_r is a reference creep rate and I_v is referred to as the viscosity index or also the Leinenkugel index [39]. For a detailed presentation of the equations of the visco-hypoplastic constitutive model, refer to Niemunis [37].

Additionally, the constitutive model was extended to be applicable under undrained conditions through the called penalty approach, according to Naylor [40]. When analysing effective stress, the rate of total stress, denoted as $\dot{\boldsymbol{\sigma}}$, is identified by combining the rate of effective stress $\dot{\boldsymbol{\sigma}}'$ with the change in pore pressure $\dot{p}_w$.

$$\dot{\boldsymbol{\sigma}} = \dot{\boldsymbol{\sigma}}' + \dot{p}_w \mathbf{I} \tag{7}$$

Assuming the velocity of the pore water to be zero, the change in pore pressure $\dot{p}_w$ can result from the state equation of pore pressures and the balance of mass.

$$\dot{p}_w = \frac{K_w}{n} \dot{\varepsilon}_v \tag{8}$$

n denotes the porosity, $\dot{\varepsilon}_v$ the deformation rate and K_w the bulk modulus of fluid. This strategy allows the computation of excess pore pressures in nearly incompressible materials based on

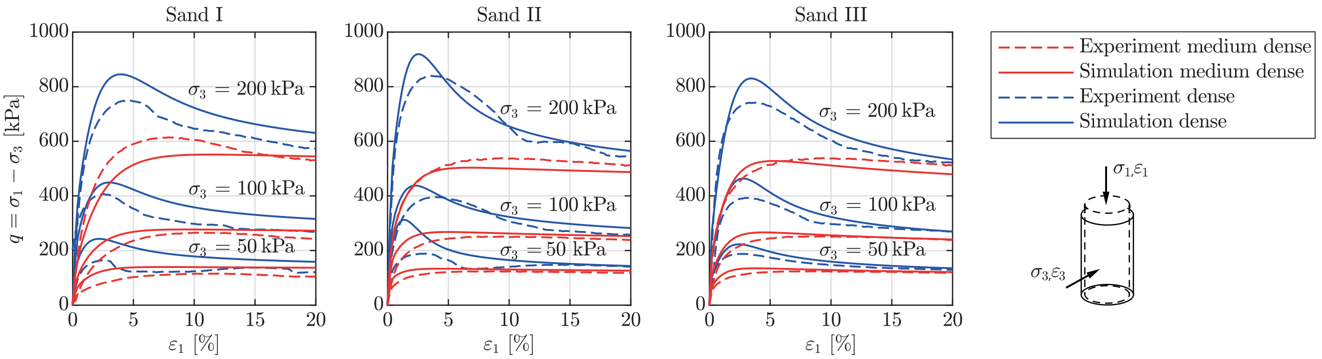

FIGURE 8 | Numerical simulations of the CD triaxial tests on medium dense ($I_D \approx 0.55$) and very dense ($I_D \approx 1.0$) samples using the determined constitutive hypoplastic parameters for Sand I (left), Sand II (middle) and Sand III (right).

effective stress parameters and an independently specified bulk modulus of fluid, which is for water $K_w = 2.08 \times 10^6$ kPa at 10°C. The chosen value of K_w is to ensure numerical stability [41].

The determination and calibration of the visco-hypoplastic model parameters proceeded as follows:

- The critical friction angle φ_c is determined through the CD triaxial test.
- The void ratio e_{100} was derived from CRS oedometer tests conducted at an average pressure of 100 kPa.
- The compression index λ and swelling index κ are obtained from CRL oedometer tests.
- The parameter β_R describes the shape of the stress path for undrained shearing and is obtained from the CU triaxial test.
- The viscosity index I_v is determined using an undrained triaxial test with a sudden jump in the deformation velocity.
- The reference deformation rate D_r is taken from auxiliary tables according to Niemunis [37].
- The additional parameters m_T, m_R, R_{max}, β_R and χ cannot be directly measured and are therefore estimated from Niemunis [37].
- The over consolidation Ratio OCR and initial void ratio e_0 values align with the initial conditions of the laboratory experiments.

The back-calculations of CRS oedometer tests using the visco-hypoplastic material model show overall satisfactory agreement between simulations and measurements for both cohesive layers in Figure 9, though some discrepancies exist in the pre-consolidation stage due to numerical limitations of the constitutive model at very low stress levels. Nevertheless, the model successfully captures the overall consolidation behaviour and provides reliable predictions for later stages.

TABLE 4 | Visco-hypoplastic parameters and state variables for the investigated cohesive soils.

Parameter	Unit	Peat	Silt
φ_c	(°)	52.4	25.95
e_{100}	(-)	2.32	0.479
λ	(-)	0.13	0.044
κ	(-)	0.046	0.014
β_R	(-)	0.95	0.95
I_v	(-)	0.07	0.025
D_r	(-)	$1.85 \cdot 10^{-6}$	$1.65 \cdot 10^{-6}$
m_T	(-)	2	2
m_R	(-)	5	5
R_{max}	(-)	$1 \cdot 10^{-4}$	$1 \cdot 10^{-4}$
β_R	(-)	0.05	0.05
χ	(-)	1	1
OCR	(-)	1.0	1.0
e_0	(-)	2.72	0.51

Table 4 offers the determined parameter sets of the visco-hypoplastic material model for the cohesive soils. It is worth mentioning that the peat's shear behaviour depends on its fibre content and degree of decomposition, resulting in high friction angles and low cohesion [42–44]. Yamaguchi [42] observed friction angles ranging from 35° to 52° in compression triaxial tests on normally consolidated peat from Japan. Ajlouni [45] reported a range of 40° to 60°. This aligns with our findings in this paper. Peat typically features large pore spaces ($e_0 = 2.72$), explaining the exceptionally high total strain observed in the CRS oedometer test.

4.3 | Numerical Modelling of CPT-Tests to Validate the Assumed Void Ratios

The void ratios for the non-cohesive soil layers, calculated using the empirical Equation (4), were used as inputs in numerical simulations of cone penetration tests (CPTs) in Figure C1 to validate their accuracy. Correctly representing the relative densities of the sand layers is essential, as they significantly influence the piles' tensile response. Therefore, validating the void ratios through numerical simulations is necessary to ensure they accurately reflect in-situ conditions. The initial void ratios of the cohesive soil layers, obtained from the undisturbed samples, were also tested in the numerical simulation. The simulations commenced from layer 2. The simulated results were then compared to

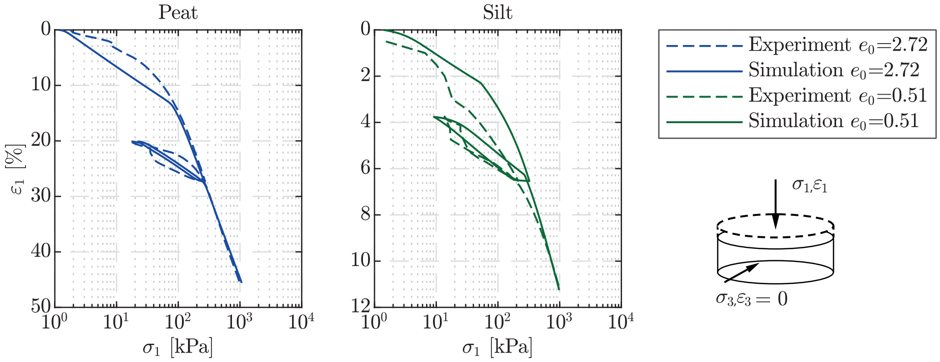

FIGURE 9 | Numerical simulations of the CRS oedometer tests on the undisturbed samples using the determined constitutive visco-hypoplastic parameters for Peat (left) and Silt (right).

the results of the CPT testing seen in Figure C2. A detailed description of the numerical model and the CPT test results is presented and discussed in Appendix C. The comparison between the field measurements and the numerical results demonstrates good agreement, validating the selected void ratios and material parameters for further simulations in the pile load tests.

5 | Numerical Simulations

Before conducting the pile load tests, a Class-A prediction is performed using Abaqus/Standard 2022 finite element program, which utilises Lagrangian elements and implicit time integration to assess the bearing capacity of the driven steel piles. Implicit time integration methods are preferred for their unconditional stability, allowing for equilibrium solutions within each increment. Consequently, larger time steps can be employed compared to explicit methods [46]. According to Dassault Systèmes [47], the size of the time step in implicit methods is typically determined based on the desired temporal resolution accuracy or the need to accurately represent non-linear processes in the numerical model. The solution of the system of equations is usually iterative. The implicit time integration method is suitable for analysing static processes and processes that occur over long periods, like pile load testing. Numerical modelling offers valuable insights into predicting the pile's ultimate pull-out bearing capacity and understanding the interactions between the pile shaft and the surrounding soil.

5.1 | Geometry and Boundary Conditions

Figure 10 illustrates the geometry of the numerical model of the pile load test, consisting of the soil entity and the pile with the relevant dimensions. Figure 10 provides a visual representation of the subsoil structure, which exhibits multi-layered soils with thin alternating sand and silt layers between 12.0 and 17.3 m. The pulling force in the model is vertical along the z-axis of the FE model. Taking advantage of the present symmetry allows for a reduction of the computational cost. Therefore, a three-dimensional quarter of the model with a length of 15 m and a height of 30 m is modelled using 160,202 continuum elements of the type C3D8R with reduced integration (1 integration point) and enhanced hourglass control to suppress any hourglass deformation modes. The C3D8R continuum elements in Abaqus are three-dimensional, eight-node linear brick elements used for modelling solid structures. The dimensions of the subsoil region correspond to a horizontal distance that is 46 times the pile width and a vertical model height that is 1.7 times the pile length. This ensures that the distance between the outer boundary of the soil region and the pile is sufficient to reduce boundary influences significantly [48]. For the quarter model of the soil, due to its inherent symmetry, X-symmetry and Y-symmetry boundary conditions are applied to the outer surfaces of the model. X-symmetry restricts movement along the x-axis and rotation around the y and z axes on one surface. Conversely, Y-symmetry limits movement along the y-axis and rotation around the x and z axes on another surface. The element size around the pile and under the pile's base matches the pile's thickness of 0.012 m. The element size gradually increases as we move vertically and horizontally from the pile. The displacements of the soil entity in the normal direction to the outer surfaces are restricted through boundary conditions to prevent that material moves out of the model.

5.2 | Modelling of the Pile

For the HP 320 × 88.5 steel pile, a linear elastic behaviour of S355 steel is assumed. The pile length in the model is 18.8 m, as the pile embeds 18.3 m into the ground and the pile head is 0.5 m above ground level. Reflecting the symmetry, only a quarter of the pile was modelled with a half web thickness in the x-direction. The same X-symmetry and Y-symmetry boundary conditions applied to the soil are also applied to the pile's outer surfaces to maintain symmetry and prevent horizontal drift. This approach ensures that the displacements perpendicular to these symmetry planes are restricted, mirroring the model's behaviour as if the entire pile and surrounding soil were present. This treatment allows us to maintain computational efficiency while accurately capturing the pile-soil interaction characteristics. The pile is modelled pre-installed into the soil, assuming 'wished in place' conditions. The pile's parameters and idealised dimensions are taken from Table 1.

5.3 | Pile-Soil Interaction

The general contact algorithm regulates the contact between the pile and the soil, utilising a surface-to-surface discretisation approach with finite sliding. For the contact in the normal

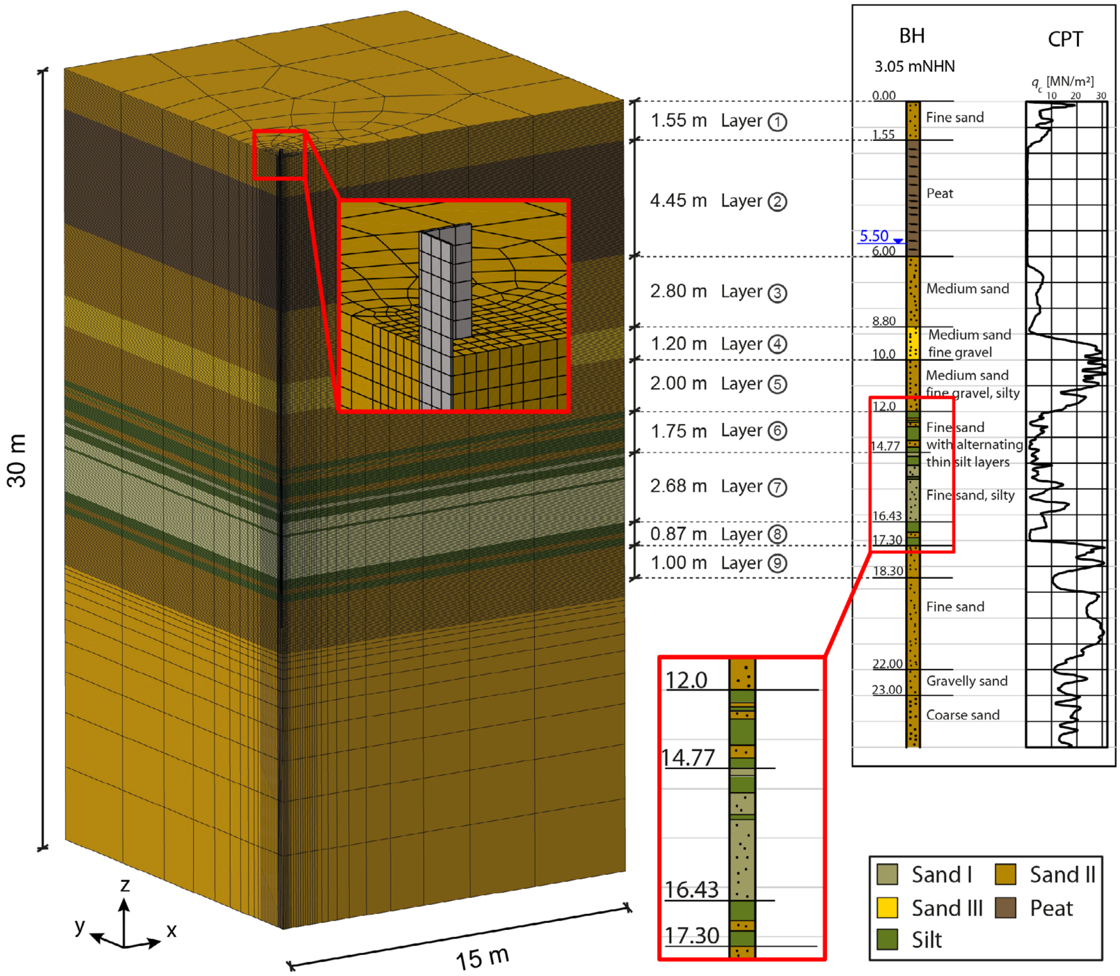

FIGURE 10 | Numerical model and discretisation of the quarter symmetric FE model for calculating the pull-out bearing capacity (left) and soil structure, along with CPT sounding results at the site of the new pile load tests (right).

direction, the hard contact formulation is applied, which does not allow the intersection of the soil and pile surfaces. The penalty method is used for constraint enforcement, with the penalty stiffness automatically determined by Abaqus. According to Coulomb's friction law, a linear elastic, ideal-plastic stick–slip model is considered in the tangential direction. The friction coefficient depends on the roughness of the pile surface and the internal friction of the surrounding soil. A friction coefficient of $\mu = \tan(2/3\varphi)$ is selected for the sands according to recommended values in [49] and [50] for non-treated rough steel surfaces. In the case of the organic peat, the literature indicates that the ratio of the interface friction angle δ to the internal friction angle φ for steel is approximately $\delta/\varphi = 1/3$ [51, 52]. Consequently, a friction coefficient of $\mu = \tan(1/3\varphi) = 0.31$ is selected for the peat layer. The friction coefficient of the thin interlayered silt layers is set to 0, as these layers are perceived to have low load-bearing capacity. In addition, these silt layers comprise only 6 % of the soil profile.

5.4 | Load History and Sequence of Steps

The initial step of the pile load testing involves establishing the geostatic stress as an initial condition. The geostatic stress is assumed to follow the K_0-distribution after Jaky [53], where the earth pressure coefficient is set at $K_0 = 1 - \sin(\varphi)$, except for peat where the value of $K_0 = 0.3$ was adopted according to Yamaguchi [42]. In the second step, the self-weight of the pile is activated, and the contact between the pile and the soil is established. In the third step, the top of the pile is subjected to an increasing vertical load according to the measurement concept, reaching 400 kN in the first cycle, then unloaded to 25 kN and subsequently reloaded in the second cycle until the pile reaches the maximum load capacity at failure. The simulation assumes ideal drainage conditions for the non-cohesive soil layers and undrained conditions for the cohesive soil layers. The pile is modelled preinstalled into the soil, assuming 'wished in place' (WIP) conditions. This approach was chosen as a pragmatic and necessary simplification for this Class-A prediction, which was formulated prior to the execution of the field tests, allowing for a focused analysis of the post-installation loaded behaviour under idealised conditions, corresponding to a pile installed with minimal imperfections.

While the WIP approach does not explicitly simulate the dynamic installation process, it is partially justified by considering the evolution of soil stresses post-installation. Pile driving is known to initially cause 'friction fatigue,' a significant reduction in

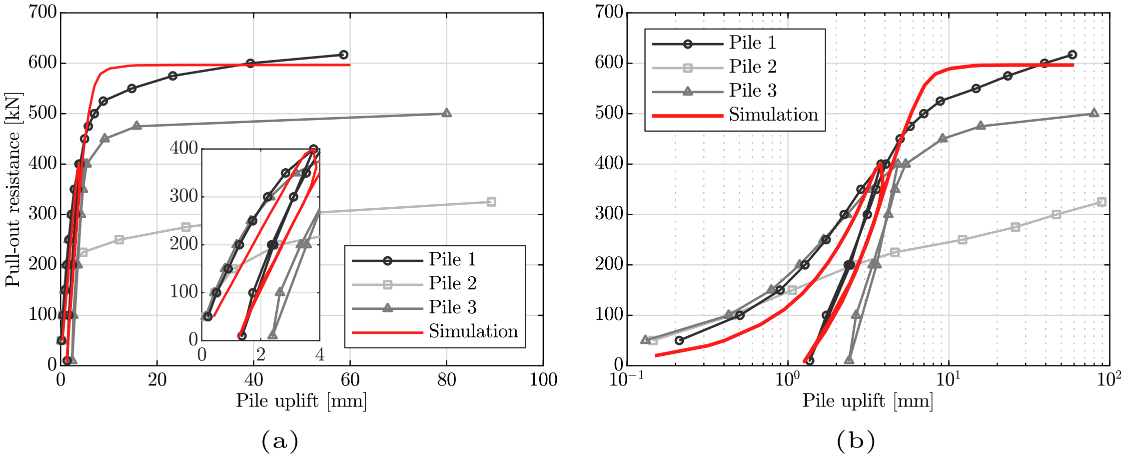

FIGURE 11 | Comparison of resistance-heave curves from pile load tests for piles 1, 2 and 3 against the numerical Class-A prediction. (a) Linear scale and (b) logarithmic scale representations of pile uplift versus applied load

effective mean stress along the pile shaft [54, 55]. This effect is observed and described in many experimental investigations of displacement pile installation [56–58], as well as many numerical simulations [59–62]. Following installation, a ‘set-up’ effect typically occurs [13, 63–65], where radial stresses around the pile gradually increase, potentially approaching at-rest earth pressure conditions [65]. The WIP model, therefore, aims to represent a plausible, stabilised stress state after these complex installation-induced phenomena have occurred. The detailed discussion of the simplifications inherent in the WIP method and the challenges of simulating the complete installation and set-up sequence are presented in Section 7.

6 | Results and Discussion

This section presents the key results from the comprehensive field pile tests and the Class-A numerical prediction. The subsequent discussion will focus on comparing these findings, starting with the methodology for quantifying the agreement between experimental and simulated data. In order to quantify the comparison between simulation and experimental results, the mean percentage error (MPE) used e. g., in Dao [66], is employed. The MPE is computed using the following formula:

$$\mathrm{MPE} = \frac{100\,\%}{n} \sum_{i=1}^{n} \left| \frac{\varepsilon_i^{\mathrm{exp}} - \varepsilon_i^{\mathrm{sim}}}{\varepsilon_i^{\mathrm{exp}}} \right| \qquad (9)$$

Here, n denotes the total number of data points. For each data point, $\varepsilon_i^{\mathrm{exp}}$ represents the corresponding experimental strain value, while $\varepsilon_i^{\mathrm{sim}}$ represents the simulated strain value. To determine the percentage error, the absolute difference between the experimental and simulated values is divided by the experimental value, and then the absolute value is taken. The result is expressed as a percentage, representing the average relative error of the simulation.

6.1 | Results of the Pile Load Testing

Figure 11 presents the resistance-heave curves from the force-controlled static tensile pile load tests in both linear (a) and semi-logarithmic scales (b). The semi-logarithmic representation in (b) provides enhanced visibility of the pile response at small displacements, particularly in the range of 0.1–10.0 mm. The test revealed varying bearing capacities among the piles: pile 1 achieved the highest bearing capacity of 617 kN and pile 2 the lowest with 325 kN. With 500 kN, the load-bearing capacity of pile 3 lies between the other two piles. Due to the different load capacities of the three piles, differing load steps are applied, as shown in Figure 12. In addition, due to its low load-bearing capacity, pile 2 was not unloaded and reloaded. The numerical model, representing an ideally installed, straight pile, serves as an idealised baseline for this Class-A prediction.

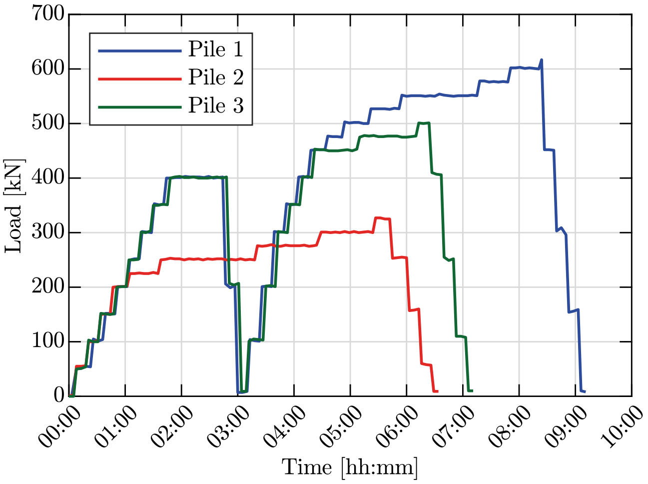

FIGURE 12 | Applied load steps during the static pile testing in the field of the three piles.

The numerical simulation demonstrates a reasonable agreement with the measured response of pile 1, although it exhibited a stiffer response than the actual test. A weighted average Mean Percentage Error (MPE) of 7.7% was calculated when comparing the simulated resistance-heave curve for pile 1 with the experimental data across the loading, unloading, and reloading stages. However, it is crucial to note that a constant load was maintained during the test at every loading phase, and the displacement creep rate of 0.1 mm in 5 min was measured. As the load approached approximately 575 kN, a significant increase in displacement creep occurred over an extended period, which, according to established testing standards, would be considered a failure. The displacement creep refers to the gradual, time-dependent movement of the pile under sustained load, which can occur even when the load does not exceed the pile's ultimate capacity. In contrast, the linear elastic-perfectly plastic ('stick-slip') Coulomb friction interface model used in the numerical simulation does not account for the creep displacement manifest in the field tests once shear stresses at the interface reach a critical threshold, resulting in a stiffer behaviour at failure compared to the field test. This idealisation is a primary contributor to the numerically stiffer prediction at failure. Neither the hypoplastic model for sands nor, more critically, the time-independent Coulomb friction model adopted for the pile-soil interface, explicitly incorporates mechanisms such as long-term interface creep-rupture or progressive softening under sustained high shear stresses approaching failure. Cyclic degradation was considered less dominant given the quasi-static nature of the loading protocol with one unload-reload cycle. Additionally, it can be observed that the recommended friction coefficients from the literature adequately predict the resistance-heave curve of pile 1. Overall, the hypoplastic and visco-hypoplastic modelling framework, after successful calibration against laboratory and CPT field data (Section 4, Appendix C), effectively captured key experimentally observed behaviours.

6.2 | Results of the Fibre-Optic Measurements

The results of the fibre-optic measurements during the pile test loads are used to analyse the different pile load-bearing capacities. Figure 13 illustrates the results of the fibre-optic strain measurements conducted on piles 1, 2 and 3. The strain values (x-coordinate) in microstrain are plotted against the depth below ground level (y-coordinate) for sensor 1, sensor 2, and the mean value obtained from both sensors. The piles have a constant cross-section and stiffness, leading to a relationship between the axial force in the pile $F(x)$ and the strain $\varepsilon(x)$ described by $F(x) = EA \cdot \varepsilon(x)$. The strain curves shown thus correspond in principle to the curve of the axial force in the pile over the depth. The gradient of the pile's strain distribution (d_ε/d_z) represents the change in axial force along the embedment length. A shallower slope in $F(x)$ or $\varepsilon(x)$ curve indicates higher skin friction, while a vertical curve corresponds to zero skin friction. In principle, with increasing load, there is an increasing strain, and accordingly, the most significant strains correspond to the load-bearing capacity.

Figure 14 presents the vertical forces computed from the measured strains at the pile head for piles 1, 2 and 3. When comparing these calculated values, derived from fibre-optic strain data, with the forces directly measured during the load tests, discrepancies of only 4.0 %, 0.5 % and 4.1 % are observed for piles 1, 2 and 3, respectively. This close agreement further underscores the reliability of the fibre-optic measurements in quantifying load transfer along the pile shaft.

However, a detailed examination of the strain measurements from sensors 1 and 2 in Figure 13 reveals an alternating strain pattern at higher load stages, especially near the piles' ultimate capacities. These measured deviations, with negative strain indicating compression in some sections, especially near the bottom of the piles, challenge the assumption of purely axial force conditions, where the axial force and strain should increase monotonically from the pile base to the pile head. These measured deviations indicate the presence of a superimposed bending component around the weak axis, which is inferred from the alternating strain pattern in the two sensors. This local bending influence is more pronounced at specific depths—particularly close to the pile tip—which is consistent with higher local soil resistance and boundary effects at the pile toe. A bending component around the strong axis of the cross-section cannot be compensated by the sensor arrangement implemented here, as additional sensors on the opposite flange would be required for such compensation. However, it is reasonable to assume that the bending component around the strong axis of the cross-section is less significant than the bending component around the weak axis.

When the measurements from both sensors are averaged, excluding pile 2, the strain ε and, correspondingly, the force F, generally increase monotonically from the pile base to the top. Figure 13 shows the average values of sensors 1 and 2 on the right-hand side. For pile 2, the most significant load transfer, indicated by the shallow slope of the strain curve, occurs between 8 and 12 m depths. Thereafter, within the multi-layered soils, the strain profile becomes nearly vertical, signifying minimal additional load transfer through skin friction. Conversely, the most notable load transfer for piles 1 and 3 is observed in the last 6 m towards the pile base, highlighting that these lower sections contribute substantially to the overall resistance. Although tensile loading dominates the general behaviour of the piles, these data show that purely axial assumptions do not fully capture the localised soil-structure interaction.

Since the load tests were carried out under vertical tension, a natural question arises regarding how tensile forces can induce bending in the pile. This can be explained by the deformation of the pile, which has been installed with locked-in bending strains, i. e., the pile is driven into the ground along a slightly curved path and then partially straightened during the load test, leading to 'corrective bending'. By separating the axial and bending components of the strain around the weak axis and calculating with the inner lever arm of the sensor paths, the acting bending moment $M(x)$ can be determined. Specifically, the mean axial strain is obtained from $\varepsilon_{\text{avg}} = (\varepsilon_1 + \varepsilon_2)/2$, while the difference $\Delta\varepsilon = \varepsilon_1 - \varepsilon_2$, along with the known sensor separation L, quantifies the curvature. The weak-axis bending moment (referenced in Figure 15) is then calculated as $M = \Delta\varepsilon / L \cdot EI$. For H-piles, this weak-axis bending, captured by the two-sensor setup, is considered the dominant component under quasi-axial loads due to the pile's lower bending stiffness around this axis, even if full 3D effects are not resolved. In Figure 15, the left-hand side shows the bending moments for piles 1, 2 and 3 at the load stage of 300 kN, the maximum load for pile 2. On the right-hand side, the moments for piles 1 and 3 at the load stage of 500 kN, which is the maximum load for pile 3, are illustrated. The relatively small derived bending moments verify that this effect occurs within the elastic range. This conclusion is supported by the calculated yield moment $M_y = \sigma_y \cdot S = 127.86$ kNm, greater than the maximum bending moment of

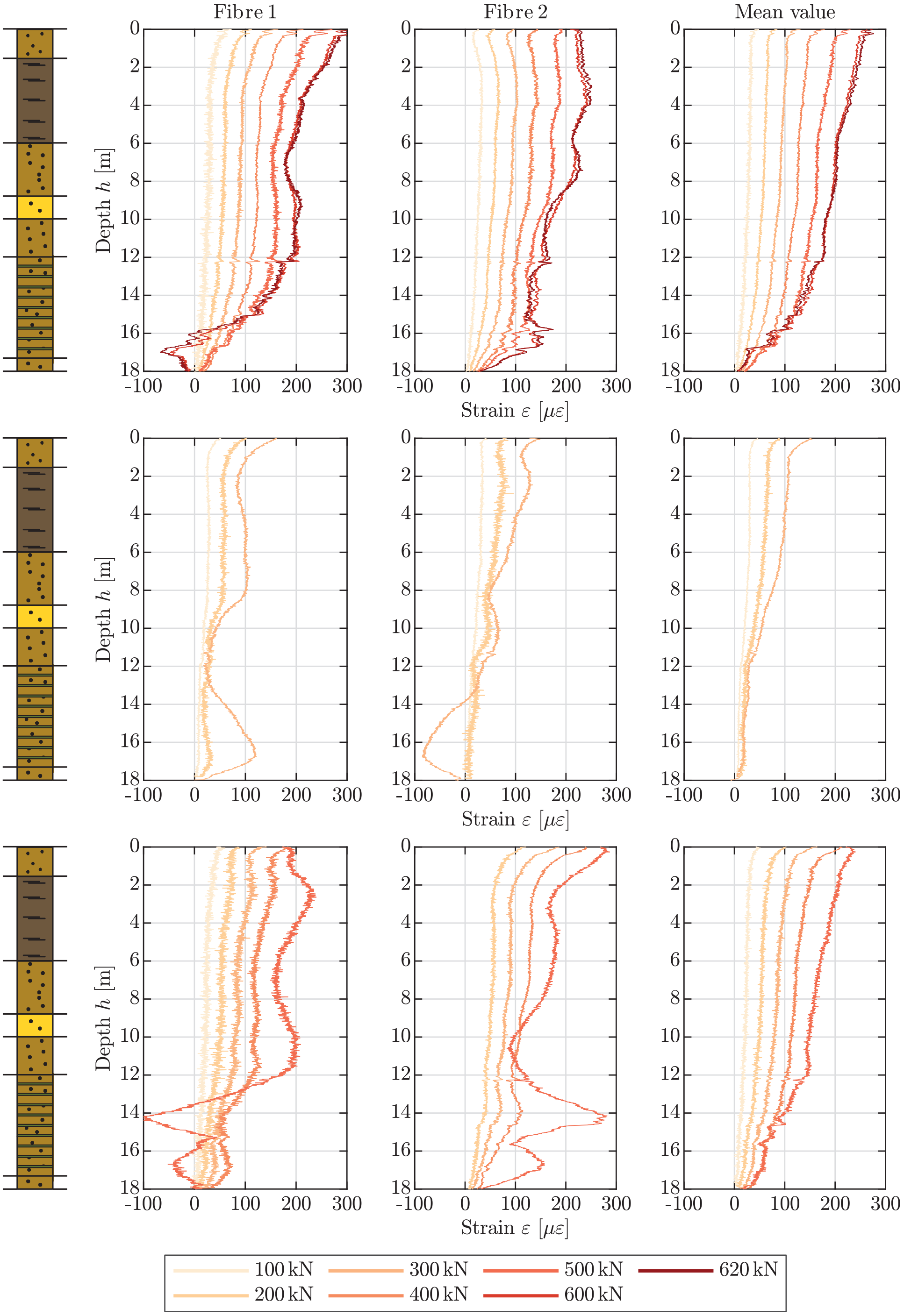

FIGURE 13 | Fibre-optic strain measurements for piles 1, 2 and 3, showing strain distributions from both individual fibres (sensor 1 and sensor 2) and their mean values. The plots illustrate the variation in axial strain (in microstrain) along the pile depth, with pile 1 reaching maximum capacity of 617 kN (top), pile 2 with limited capacity of 325 kN (middle), and pile 3 achieving intermediate capacity of 500 kN (bottom).

19.95 kNm. Here, σ_y denotes the yield stress, and S represents the elastic section modulus.

The described corrective bending effect only becomes significant at higher load levels and correlates with a pile displacement exceeds the creep rate of 2 mm/log cycle of time. This phenomenon can be explained by the behaviour of the piles during the pile load test. When piles experience high creep displacement, they are progressively and rapidly pulled out of the soil under constant load. As a result, the piles encounter greater constraints and, consequently, higher corrective bending. This occurs because the pile deforms and attempts to return to its original state through elasticity. According to the measurement report, pile 2 exhibits a creep value K_s exceeding 10 mm at the 300 kN load level, whereas piles 1 and 3 have a K_s value below 0.5 mm at the same load level.

Comparing the axial and bending components of the strain in the manner described for the highest load level achieved for pile 2

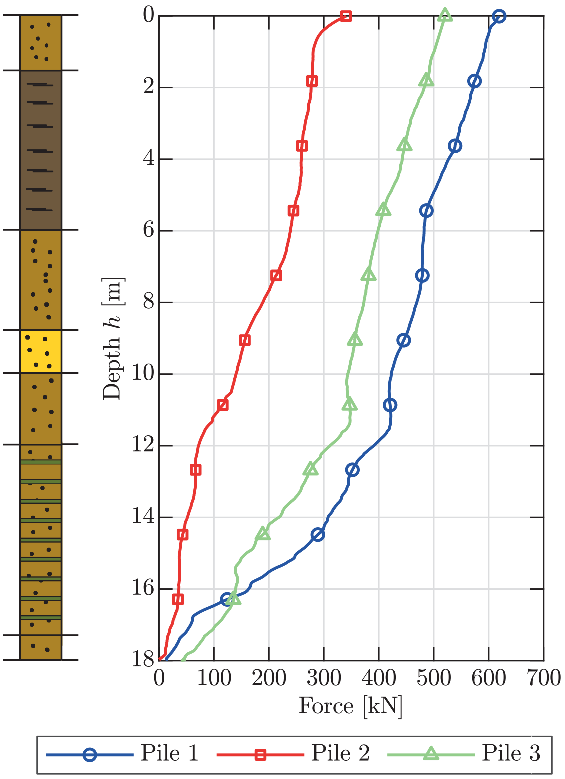

FIGURE 14 | Axial forces in piles 1, 2 and 3 calculated from fibre-optic strain measurements. The forces are plotted against depth, illustrating the load distribution along the pile length during tensile loading.

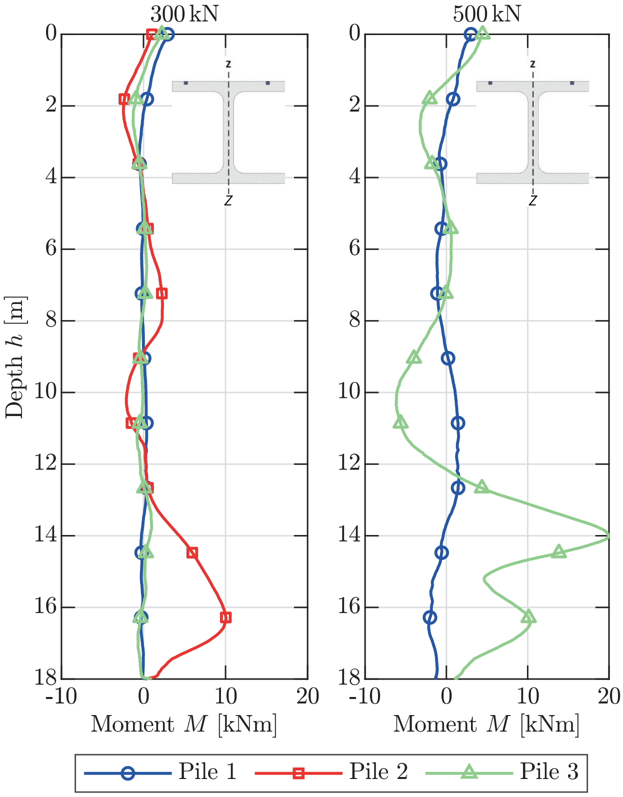

FIGURE 15 | Bending moments around the weak axis z–z at the load stages 300 kN (left) and 500 kN (right) for the three investigated piles.

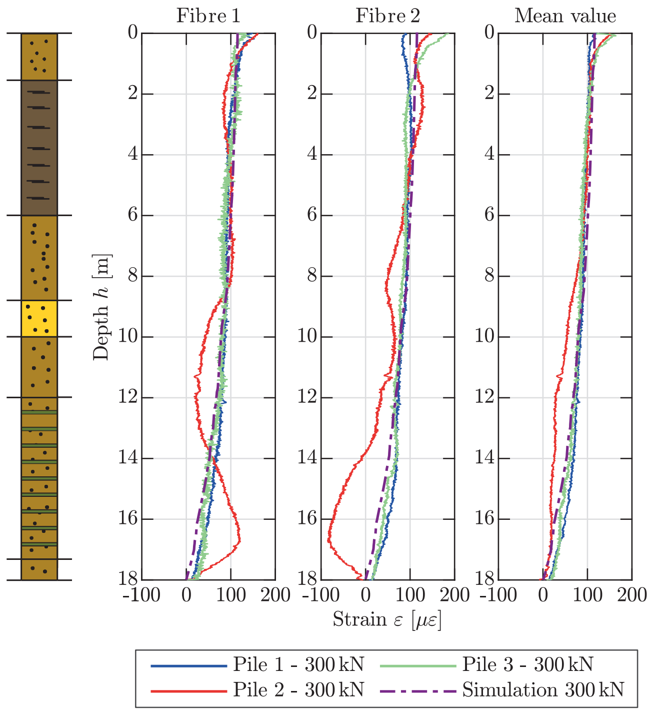

FIGURE 16 | Results of the fibre-optic strain measurements for the three investigated piles at 300 kN load stage compared with the numerical simulation.

(F = 300 kN, see Figure 16), the correlation between a strong bending component and a lower load-bearing capacity becomes particularly evident.

The simulated strain distributions of pile 1 during the 300 and 600 kN load stages are in good agreement with the results of the field test, as shown in Figure 17. Indeed, pile 1, with minimal inferred bending and the highest capacity, aligned well with the idealised numerical model (Figure 11 and Figure 17). In contrast, the lower capacities and complex strain patterns of Piles 2 and 3 (Figure 13) are attributed to substantial measured locked-in bending strains from installation imperfections (Figure 15). Such pre-existing geometric imperfections, and their consequent non-monotonic strains, cannot be replicated by an idealised straight-pile model; its comparison to Piles 2 and 3 thus highlights the significant negative impact of installation-induced deformation. The mean percentage errors (MPE) of the simulated strain distributions of pile 1 during the 300 and 600 kN load stage are calculated to be 7.23 % and 12.8 %, respectively. this level of agreement for detailed strain profiles is often considered reasonable for a Class-A prediction in such complex geotechnical systems.

When the maximum shear stress is fully activated along the entire embedded length, the ultimate pull-out load of 617 kN is attained. As expected, the most significant strain gradient is between 12 and 18 m below ground level. The simulation results confirm the assumption mentioned earlier that pile 1 does not exhibit any considerable bending component (compare with Figure 15), since the simulation models the pile as 'wished in place' without bending or imperfections. This further emphasises that the deformations occurring during the driving process of

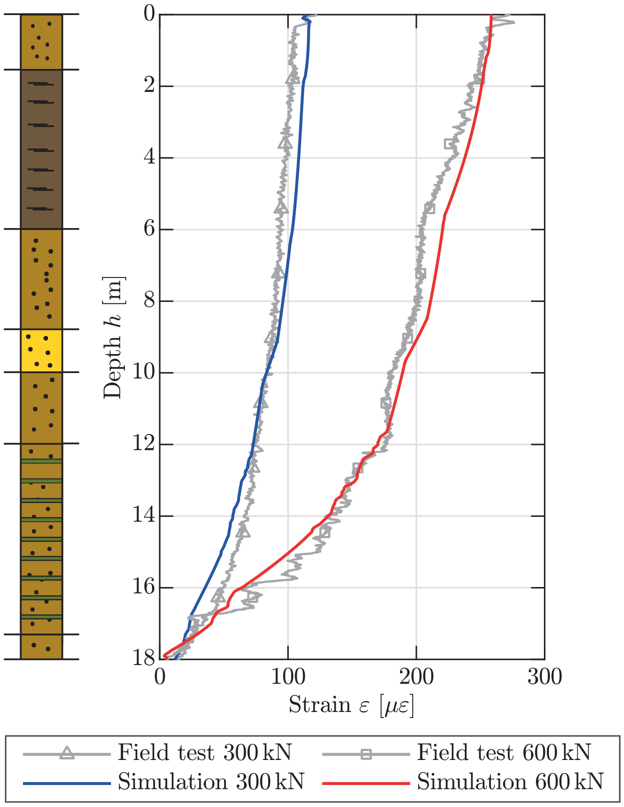

FIGURE 17 | Simulated and measured strain distributions of pile 1 for the load stages 300 and 600 kN.

the piles significantly impact their subsequent bearing capacity. Considering that the piles were installed in similar soil conditions, it is plausible to conclude that the installation process and the resulting locked-in bending strains primarily caused the different load-bearing capacities of the piles. While concurrent soil disturbance undoubtedly occurs during installation and contributes to performance differences, this study focused on the quantifiable impact of geometric imperfections (locked-in bending) as a primary driver for the observed 60% variance in capacity among adjacent piles, despite identical installation procedures and assumed consistent soil. Adjustments in the pile alignment during driving could introduce soil structure distortion near the pile shaft, which could form a wave-like driving channel and bending constraints in the pile. Any minor misalignment or eccentricity in the pile installation becomes more pronounced near the base due to the cumulative effect of installation-induced deformations along the pile length. Furthermore, the presence of thinly inter-layered soils near the pile base creates heterogeneous resistance patterns that can amplify localised bending effects.

To optimise pile performance, maintaining a consistent driving inclination (within acceptable limits) is preferable to attempting corrections that might introduce bending constraints. Implementation of low-impact installation methods and enhanced pile-driving guidance systems could minimise these installation-induced effects. These findings emphasise the critical importance of installation quality control in achieving designed pile capacities, particularly in complex soil conditions.

7 | Limitations

This study, while providing valuable insights into tension pile behaviour in thinly inter-layered soils and the impact of installation imperfections, has several inherent limitations, particularly within its Class-A prediction framework. A key simplification was the Wished-in-Place (WIP) pile installation assumption. Common for predictive analyses, especially Class-A predictions formulated with pre-field test uncertainties, this approach was adopted to establish an idealised baseline for the post-installation loaded behaviour, corresponding to a pile installed with minimal imperfections. It does not explicitly simulate dynamic installation effects like soil displacement, changes in soil stress state (e. g., radial stress degradation or densification), or subsequent time-dependent set-up phenomena (such as those occurring during the 5 weeks post-installation in this study); consequently, unquantified soil disturbance due to installation variability could also contribute to the observed differences in pile performance alongside the measured locked-in bending. Simulating these complex installation effects, which often require sophisticated numerical techniques to capture phenomena like complex time-dependent set-up, under Class-A predictive constraints was deemed impractical due to the numerous additional assumptions required. Additionally, the sometimes inconclusive or contradictory findings in literature regarding the precise influence of different installation methods on pile capacity and load transfer mechanisms (e. g., studies by [67, 68] in contrast to [69, 70]) further complicate predictive modelling efforts. Furthermore, the pile-soil interface was modelled using a time-independent Coulomb friction law, which omits complex behaviours such as stress- and density-dependency or interface creep, contributing to discrepancies like the numerically stiffer response at failure. The scope of the bending analysis, using two sensors on a single flange, quantified weak-axis bending–argued as dominant for an H-pile under quasi-axial tension–but a more extensive sensor array would be needed for a full 3D bending analysis, including strong-axis bending and torsion. These limitations highlight areas for future research, including the incorporation of more sophisticated installation process simulations (e. g., using coupled Eulerian-Lagrangian or Material Point Methods) and advanced interface models (e. g., using hypoplastic contact model).

8 | Conclusions and Outlook

The study presents a comprehensive investigation into the bearing capacities of tension steel piles in thinly inter-layered soils, utilising field measurements and a numerical Class-A prediction. The research was driven by significant discrepancies between predicted and actual bearing capacities during pile testing, highlighting the limitations of commonly used analytical methods. A large-scale field test involving three adjacent tension steel piles provided valuable measurements, including innovative fibre-optic strain monitoring. The numerical model utilised hypoplastic and visco-hypoplastic constitutive models to capture the complex interactions between the piles and the varying soil layers. This study contributes to a better understanding of pile behaviour under tension load in thinly inter-layered soils, which is, to the authors' knowledge, a rarely explored area in the existing literature.

The pile load testing results showed significant variations in the bearing capacities among the piles, which is primarily attributed to the installation process, with the least impacted pile 1 achieving a maximum bearing capacity of 617 kN, compared to the most affected pile 2, which only reached 325 kN.

The numerical model successfully predicted the ultimate load capacity of pile 1 before conducting the field tests, providing valuable insights into the interactions between the pile and the soil and a complement to the experimental data. The simulated strain distributions showed good agreement with field measurements, indicating that the model effectively captures the essential mechanics of pile-soil interaction in thinly inter-layered soils for an ideally installed pile. However, the model's use of the 'wished in place' assumption, chosen for simplicity within the Class-A prediction framework and due to technical complexities of simulating full installation and set-up, may not capture all dynamic soil-pile interactions, potentially impacting FEM result accuracy. This limitation is recognised, and further validation and refinement of this assumption and interface modelling are recommended to improve numerical model reliability.

Fibre-optic measurements indicated the presence of locked-in bending strains post-installation, especially in piles 2 and 3. This bending component is attributed to the deformation of the piles during installation, and the calculated bending moments confirmed the presence of the bending strain within the elastic range. The calculated vertical forces in the piles correspond with the measured forces from the load testing, which supports the reliability of the fibre-optic strain data. A notable correlation was found between significant bending strains and reduced load-bearing capacities of the piles, explaining the variance in their bearing capacities and the impact of the installation-induced strains on pile performance. The study distinguishes between the measured impact of these geometric imperfections (bending) as a direct consequence of installation variability, and the acknowledged but unquantified concurrent soil disturbance effects, also stemming from the installation process.

The research contributes to a deeper understanding of tension pile behaviour in complex soil conditions and underscores the necessity of considering installation effects in pile design. It also emphasises the potential of advanced measurement techniques, like fibre-optic sensing, in providing detailed insights into pile behaviour, thereby aiding in developing more accurate predictive models and design methodologies in geotechnical engineering.

Further research could incorporate advanced measurement techniques during pile installation, such as fibre-optic measurements, to identify and evaluate the deformation and strain distribution in the pile. This allows for a thorough understanding of pile behaviour and provides insights into improving the accuracy and efficiency of the installation process. Additionally, it would be beneficial to investigate various installation methods, especially those with minimal induced deformation of the piles, and their impact on the tensional bearing capacity. Building upon the diagnostic capabilities and mechanistic understanding presented, future research should also aim to develop quantitative design guidelines and actionable thresholds correlating the magnitude of installation-induced imperfections (like locked-in bending strains) with expected reductions in pile capacity. This would typically require systematic investigations, potentially involving laboratory or centrifuge model tests under controlled conditions, to establish more generalised predictive relationships. Another focus could involve numerical constitutive contact modelling, which is crucial for accurately predicting pile axial loading. While the Coulomb interface model is commonly used in geotechnical analyses and was sufficient for the presented case as a baseline, the complexity of soil-structure interfaces, particularly concerning time-dependent phenomena like creep and softening, could sometimes surpass what can be captured by this model. The implementation of more sophisticated constitutive contact models will be addressed in subsequent research to better capture the complex mechanical behaviour at the soil-pile interface. Nevertheless, this study showed a successful Class-A prediction in the complex, thinly inter-layered soil of a pile, properly installed. The study highlighted the significant impact of installation methods on the pile's performance, especially in soils with multiple thin layers. The findings advocate optimising installation techniques to minimise bending strains and enhance pile load-bearing capacities.

Author Contributions

Diaa Alkateeb: conceptualisation, methodology, software, validation, formal analysis, investigation, data curation, writing - original draft, writing - review and editing, visualisation, project administration. **Jürgen Grabe:** conceptualization, supervision, writing - review and editing, funding acquisition.

Acknowledgments

This work was conducted as part of the R&D project 'Tragfähigkeit von Stahlrammpfählen' in collaboration with the federal waterways engineering and research institute (BAW). We extend our gratitude to the BAW for their financial support. Additionally, we appreciate SENSICAL for their assistance in instrumenting the fibre-optics and providing the measurements.

Open access funding enabled and organized by Projekt DEAL.

Conflicts of Interest

The authors declare no potential conflict of interests.

Data Availability Statement

Some or all data, models, or codes that support the findings of this study are available from the corresponding author upon reasonable request.

References

1. EA-Pfähle, *Recommendations on Piling (EA-Pfähle)*, 1st ed. (Wiley, 2013), https://doi.org/10.1002/9783433604113.

2. I. Herle, "Numerical Predictions and Reality," *Lecture Notes in Applied and Computational Mechanics* 13 (2003): 167–194, https://doi.org/10.1007/978-3-540-45079-57.

3. T. Lambe, "Predictions in Soil Engineering," *Géotechnique* 23, no. 2 (1973): 149–202, https://doi.org/10.1680/geot.1973.23.2.151.

4. M. Witzel, "Zur Tragfähigkeit Und Gebrauchstauglichkeit von Vorgefertigten Verdrängungspfählen in Bindigen Und Nichtbindigen Böden" (PhD diss., Universität Kassel, 2004).

5. R. Jardine, *ICP Design Methods for Driven Piles in Sands and Clays* (Thomas Telford and Imperial College, 2005).

6. J. Quarg-Vonscheidt, "Berechnungsmodell Für Die Tragfähigkeit Und Das Gruppenverhalten von Zugpfählen" (PhD diss., Bergische Universität Wuppertal, 2000).

7. P. Robertson and K. Cabal, *Guide to Cone Penetration Testing for Geotechnical Engineering*, 6th ed. (Gregg Drilling & Testing, Inc., 2015).

8. D. Alkateeb and J. Grabe, "On the Application of Analytical Methods and Empirical Values for the Determination of the Pull-out Resistance of Driven Steel Piles," in *Proceedings of 10th International Conference on Physical Modelling in Geotechnics (ICPMG) 2022 in Daejon/Korea* (Korea Geotechnical Society, 2022), 844–848.

9. K. Gwizdala, "Polish Design Methods for Single Axially Loaded Piles," in *Design of Axially Loaded Piles - European Practice* (CRC Press, 1997).

10. S. Prakash and H. D. Sharma, *Pile Foundations in Engineering Practice* (John Wiley & Sons, 1990).

11. M. Bustamante and R. Frank, "Design of Axially Loaded Piles—French Practice," in *Design of Axially Loaded Piles - European Practice* (CRC Press, 1997).

12. A. Holeyman, C. Bauduin, M. Bottiau, et al., "Design of Axially Loaded Piles—Belgian Practice," in *Design of Axially Loaded Piles - European Practice* (CRC Press, 1997).

13. R. Skov, "Pile Foundation—Danish Design Methods and Piling Practice," in *Design of Axially Loaded Piles - European Practice* (CRC Press, 1997).

14. I. Manoliu, "Design of Axially Loaded Piles—Romanian Practice," in *Design of Axially Loaded Piles - European Practice* (CRC Press, 1997).

15. A. S. Simonsen and C. Athanasiu, "Design of Axially Loaded Piles—Norwegian Practice," in *Design of Axially Loaded Piles - European Practice* (CRC Press, 1997).

16. API, *Recommended Practice for Planning, Designing and Constructing Fixed Offshore Platforms—Working Stress Design*, 21 ed. (American Petroleum Institute, 2002).

17. J. De Kuiter and F. L. Beringen, "Pile Foundations for Large North Sea Structures," *Marine Georesources & Geotechnology* 3, no. 3 (1979): 267–314, https://doi.org/10.1080/10641197909379805.

18. A. De Nicola and M. F. Randolph, "Tensile and Compressive Shaft Capacity of Piles in Sand," *Journal of Geotechnical and Geoenvironmentral Engineering* 119, no. 12 (1993): 1952–1973, https://doi.org/10.1061/(ASCE)0733-9410(1993)119:12(1952).

19. M. F. Randolph, "Science and Empiricism in Pile Foundation Design," *Géotechnique* 53, no. 10 (2003): 847–875, https://doi.org/10.1680/geot.2003.53.10.847.

20. B. M. Lehane, R. J. Jardine, A. J. Bond, and R. Frank, "Mechanisms of Shaft Friction in Sand From Instrumented Pile Tests," *Journal of Geotechnical Engineering, ASCE* 119, no. 1 (1993): 19–35, https://doi.org/10.1061/(ASCE)0733-9410(1993)119:1(19).

21. T. I. van der Linden, D. A. de Lange, and M. Korff, "Cone Penetration Testing in Thinly Inter-Layered Soils," *Proceedings of the Institution of Civil Engineers - Geotechnical Engineering* 171, no. 3 (2018): 215–231, https://doi.org/10.1680/jgeen.17.00061.

22. H. Kaya, "Bodenverschleppung und Spaltbildung infolge der Einbringung von Profilen in Dichtungsschichten aus Ton" (PhD diss., Technische Universität Hamburg-Harburg, 2016).

23. K. Emmett, "Pile Disturbance in Layered Ground," *Ground Engineering* 38, no. 12 (2005): 30–32.

24. D. A. De Lange, J. Terwindt, and T. I. Van der Linden, "CPT in Thinly Inter-Layered Soils," in *Cone Penetration Testing 2018*, eds. J. Peuchen, F. Pisanò, and M. A. Hicks (CRC Press, 2018), 383–388.

25. L. Fenu, E. Congiu, M. Deligia, G. F. Giaccu, A. Hosseini, and M. Serra, "Buckling Analysis of Piles in Multi-Layered Soils," *Applied Sciences* 11, no. 22 (2021): 10624, https://doi.org/10.3390/app112210624.

26. R. Ofner and H. Wimmer, "Knicknachweis von Mikropfählen in Geschichteten Böden," *Bautechnik* 84 (December 2007): 881–890, https://doi.org/10.1002/bate.200710075.

27. H.-G. Kempfert and C. Moormann, "Pfahlgründungen," in *Grundbau-Taschenbuch*. ch. 3.2 (John Wiley & Sons, Ltd, 2018), 79–323.

28. B. Mazurkiewicz, "Einfluss von Rammgeräten auf die Tragfähigkeit von Stahlbetonpfählen," in *Symposium Pfahlgründungen, Darmstadt* (Technical University of Darmstadt, 1986), 31–36.

29. The Overseas Coastal Area Development Institute of Japan, *Technical Standards and Commentaries for Port and Harbour Facilities in Japan* (The Overseas Coastal Area Development Institute of Japan, 2002).

30. W. Eickhoff and R. Ulrich, "Optical Frequency Domain Reflectometry in Singlemode Fiber," *Applied Physics Letters* 39, no. 9 (1981): 693–695, https://doi.org/10.1063/1.92872.

31. J. Nakayama, K. Iizuka, and J. Nielsen, "Optical Fiber Fault Locator by the Step Frequency Method," *Applied Optics* 26, no. 3 (1987): 440, https://doi.org/10.1364/ao.26.000440.

32. M. Weisbrich, "Verbesserte Dehnungsmessung im Betonbau Durch Verteilte Faseroptische Sensorik" (PhD diss., TU Bergakademie Freiberg, 2021).

33. A. Künzel, "Parameteridentifikation auf Basis Faseroptisch Gemessener Quasi-Kontinuierlicher Dehnungssignale" (PhD diss., Technische Universitaet Berlin, 2016).

34. F. H. Kulhawy and P. H. Mayne, *Manual on Estimating Soil Properties for Foundation Design* (Electric Power Research Institute, 1990).

35. P.-A. von Wolffersdorff, "A Hypoplastic Relation for Granular Materials With a Predefined Limit State Surface," *Mechanics of Cohesive-frictional Materials* 1, no. 3 (1996): 251–271, https://doi.org/10.1002/(SICI)1099-1484(199607)1:3<251::AID-CFM13>3.0.CO;2-3.

36. A. Niemunis and I. Herle, "Hypoplastic Model for Cohesionless Soils With Elastic Strain Range," *Mechanics of Cohesive-frictional Materials* 2, no. 4 (1997): 279–299, https://doi.org/10.1002/(SICI)1099-1484(199710)2:4%3C279::AID-CFM29%3E3.0.CO;2-8.

37. A. Niemunis, "Extended Hypoplastic Models for Soils" (PhD diss., Ruhr-Universität, 2003).

38. F. Norton, *The Creep of Steel at High Temperatures*, ser. Bulletin (McGraw-Hill book Company, Incorporated, 1929).

39. H. J. Leinenkugel, "Deformations- und Festigkeitsverhalten bindiger Erdstoffe. Experimentelle Ergebnisse und ihre physikalische Deutung" (PhD diss., University of Karlsruhe, 1976).

40. D. J. Naylor, "Stresses in Nearly Incompressible Materials by Finite Elements With Application to the Calculation of Excess Pore Pressures," *International Journal for Numerical Methods in Engineering* 8, no. 3 (1974): 443–460, https://doi.org/10.1002/nme.1620080302.

41. G. Qiu, "Coupled Eulerian Lagrangian Simulations of Selected Soil-Structure Interaction Problems" (PhD diss., Technische Universität Hamburg-Harburg (TUHH), 2012).

42. Y. Yamaguchi, Y. Ohira, K. Kogure, and S. Mori, "Undrained Shear Characteristics of Normally Consolidated Peat Under Triaxial Compression and Extension Conditions," *Soils and Foundations* 25, no. 3 (1985): 1–18, https://doi.org/10.3208/sandf1972.25.31.

43. T. B. Edil and A. W. Dhowian, "At-Rest Lateral Pressure of Peat Soils," *Journal of the Geotechnical Engineering Division, ASCE* 107, no. 2 (1981): 201–217, https://doi.org/10.1061/AJGEB6.0001097.

44. S. Cola and G. Cortellazzo, "The Shear Strength Behavior of two Peaty Soils," *Geotechnical and Geological Engineering* 23 (2005) 679–695, https://doi.org/10.1007/s10706-004-9223-9.

45. G. Mesri and M. Ajlouni, "Engineering Properties of Fibrous Peats," *Journal of Geotechnical and Geoenvironmental Engineering* 133, no. 7 (July 2007), https://doi.org/10.1061/(ASCE)1090-0241(2007)133:7(850).

46. K.-J. Bathe, *Finite Element Procedures* (Massachusetts Institute of Technology, 2006).

47. Dassault Systèmes, *Simulia User Assistance 2020 – Abaqus Documentation* (Dassault Systèmes Simulia Corp., 2020).

48. EANG, *Empfehlungen Des Arbeitskreises Numerik in Der Geotechnik* (Wiley/Deutsche Gesellschaft für Geotechnik and Wilhelm Ernst & Sohn, 2014).

49. *Recommendations of the Committee for Waterfront Structures Harbours and Waterways: EAU 2020*, 10th ed. (Wilhelm Ernst & Sohn/EAU, December 2023).

50. DIN 4085:2017-08, "Baugrund - Berechnung des Erddrucks," (Beuth Verlag GmbH, 2017).

51. H. Canakci, M. Hamed, F. Celik, W. Sidik, and F. Eviz, "Friction Characteristics of Organic Soil With Construction Materials," *Soils and Foundations* 56, no. 6 (2016): 965–972, https://doi.org/10.1016/j.sandf.2016.11.002.

52. B. Ampera and T. Aydogmus, "Skin Friction Between Peat and Silt Soils With Construction Materials," *Electronic Journal of Geotechnical Engineering* 10 (January 2005).

53. J. Jaky, "Pressure in Silos," in *Proceedings of the 2nd International Conference on Soil Mechanics and Foundation Engineering* 1 (International Society for Soil Mechanics and Geotechnical Engineering, 1948), 103–107.

54. E. P. Heerema, "Predicting Pile Driveability: Heather as an Illustration of the 'Friction Fatigue' Theory," in *Society of Petroleum Engineers - SPE European Petroleum Conference* 13 (1978): 413–422.

55. A. J. Bond and R. J. Jardine, "Effects of Installing Displacement Piles in a High OCR Clay," *Geotechnique* 41, no. 3 (1991): 341–363, https://doi.org/10.1680/geot.1991.41.3.341.

56. D. J. White and M. D. Bolton, "Displacement and Strain Paths During Planestrain Model Pile Installation in Sand," *Geotechnique* 54, no. 6 (2004): 375–397, https://doi.org/10.1680/geot.2004.54.6.375.

57. Z. Yang, R. Jardine, B. Zhu, C. Tsuha, and P. Foray, "Sand Grain Crushing and Interface Shearing During Displacement Pile Installation in Sand," *Geotechnique* 60, no. 6 (2010): 469–482, https://doi.org/10.1680/geot.2010.60.6.469.

58. M. Randolph and S. Gourvenec, *Offshore Geotechnical Engineering* (CRC Press, July 2017).

59. S. Henke, "Herstellungseinflüsse aus Pfahlrammung im Kaimauerbau" (PhD diss., Veröffentlichungen des Instituts für Geotechnik und Baubetrieb der Technischen Universität Hamburg-Harburg / Technische Universität Hamburg-Harburg (TUHH), 2008).

60. E. Heins and J. Grabe, "Class-A-prediction of Lateral Pile Deformation With Respect to Vibratory and Impact Pile Driving," *Computers and Geotechnics* 86 (2017): 108–119.

61. P. Staubach, J. Machaček, R. Sharif, and T. Wichtmann, "Back-Analysis of Model Tests on Piles in Sand Subjected to Long-Term Lateral Cyclic Loading: Impact of the Pile Installation and Application of the HCA Model," *Computers and Geotechnics* 134 (2021): 104018, https://doi.org/10.1016/j.compgeo.2021.104018.

62. P. Staubach, J. Machaček, M. Moscoso, and T. Wichtmann, "Impact of the Installation on the Long-Term Cyclic Behaviour of Piles in Sand: A Numerical Study," *Soil Dynamics and Earthquake Engineering* 138 (2020): 106223, https://doi.org/10.1016/j.soildyn.2020.106223.

63. F. C. Chow, R. J. Jardine, J. F. Nauroy, and F. Brucy, "Time-Related Increase in Shaft Capacities of Driven Piles in Sand," *Géotechnique* 47, no. 2 (1997): 353–361.

64. G. Axelsson, "Long-Term set-up of Driven Piles in Non-Cohesive Soils" (PhD diss., Royal Institute of Technology, Division of Soil and Rock Mechanics, Department of Civil and Environmental Engineering, 2000).

65. J. Grabe, P. Busch, and T. Hamann, "On the Set-Up of Piles," in *International Conference on Offshore Mechanics and Arctic Engineering* vol. 3 (Offshore Geotechnics, June 2014).

66. D. A. Dao, D. Alkateeb, and M. Schröder, "Discrepancies Between Element Tests and Large-Scale LDFE Simulations: A Case Study on Anchor Kinematics During Installation in Clay," *Computers and Geotechnics* 163 (2023): 105698, https://doi.org/10.1016/j.compgeo.2023.105698.

67. J.-L. Briaud, H. M. Coyle, and L. M. Tucker, "Axial Response of Three Vibratory-and Three Impact-Driven H Piles in Sand," *Transportation Research Record* no. 1277 (1990).

68. R. L. Mosher, "Axial Capacity of Vibratory-Driven Piles Versus Impact-Driven Piles," no. 1277 (Committee on Foundations of Bridges and Other Structures, 1990).

69. C. Vipulanandan, D. Wong, and M. W. O'Neill, "Behavior of Vibro-Driven Piles in Sand," *Journal of Geotechnical Engineering* no. 116, No.8 (1990): 1211–1230, https://doi.org/10.1061/(ASCE)0733-9410(1990)116:8(1211).

70. S. Borel, M. Bustamante, and F. Rocher-Lacoste, "The Comparative Bearing Capacity of Vibratory and Impact Driven Piles," in *Transvib 2006* eds. G. Holeyman and F. Rocher-Lacoste (CRC Press, 2006).

71. M. E. Mabsout and J. L. Tassoulas, "A Finite Element Model for the Simulation of Pile Driving," *International Journal for Numerical Methods in Engineering* 37, no. 2 (1994): 257–278, https://doi.org/10.1002/nme.1620370206.

72. DIN EN ISO 22476-1, "Geotechnical Investigation and Testing - Field Testing - part 1: Electrical Cone and Piezocone Penetration Test (ISO 22476-1:2012 + cor. 1:2013); German Version EN ISO 22476-1:2012 + AC:2013," (Beuth Verlag GmbH, 2013).

Appendix A: Soil Parameters of the Four Investigated Sites

The following table presents the soil parameters derived from the evaluation of cone penetration testing (CPT) data at the four investigated sites. The soil profile at each site is divided into several layers, and the corresponding properties are provided for each layer. These properties include layer thickness, unit weight (γ), cone resistance (q_c), relative density (I_D), friction angle (φ'), mean grain size (d_{50}), shear modulus (G), undrained shear strength (S_u), soil behaviour type index (I_c), and plasticity index (I_p). This detailed characterisation of the soil conditions is crucial for interpreting the pile behaviour and for the analytical predictions discussed in the main text of the paper. It is worth mentioning that the averaged actual measured capacities of the piles at each site were 473, 449, 353 and 480 kN for sites 1, 2, 3 and 4. respectively.

Appendix B: Equations of the Hypoplastic Model With Intergranular Strain Extension

The hypoplastic constitutive law is given by:

$$\dot{\boldsymbol{\sigma}} = \mathrm{f}(\boldsymbol{\sigma}', \dot{\varepsilon}, e) \ , \tag{B1}$$

where $\dot{\boldsymbol{\sigma}}$ represents the stress rate tensor, $\boldsymbol{\sigma}'$ defines the effective stress tensor, $\dot{\varepsilon}$ stands for the deformation rate tensor, and e symbolises the void ratio. The formulation, according to von Wolffersdorff [35], is expressed as follows:

$$\dot{\boldsymbol{\sigma}} = \mathsf{L} : \dot{\varepsilon} + \mathsf{N}\|\dot{\varepsilon}\| \ . \tag{B2}$$

Here, L and N symbolise linear and non-linear components of stiffness, respectively, both dependent on stress and void ratio, and are detailed as:

$$\mathsf{L} = f_b f_e \frac{1}{\mathrm{tr}(\hat{\boldsymbol{\sigma}} \cdot \hat{\boldsymbol{\sigma}})} (F_l^2 \mathbf{I} + a_l^2 \hat{\boldsymbol{\sigma}}\hat{\boldsymbol{\sigma}}) \tag{B3}$$

$$\mathsf{N} = f_b f_e f_d \frac{F_l a_l}{\mathrm{tr}(\hat{\boldsymbol{\sigma}} \cdot \hat{\boldsymbol{\sigma}})} (\hat{\boldsymbol{\sigma}} + \hat{\boldsymbol{\sigma}}^*) \tag{B4}$$

with $\hat{\boldsymbol{\sigma}} = \frac{\boldsymbol{\sigma}'}{\mathrm{tr}\boldsymbol{\sigma}'}$ and $\hat{\boldsymbol{\sigma}}^* = \hat{\boldsymbol{\sigma}} - \frac{1}{3}\mathbf{I}$. The scalar factors are defined by:

TABLE A1 | Soil parameters from the evaluation of the cone penetration testing data (CPT) of the four investigated sites.

Layer	Thickness	$\gamma \left(\frac{\text{kN}}{\text{m}^3}\right)$	q_c (MPa)	I_D (-)	φ' (°)	d_{50} (mm)	G (MPa)	S_u (kPa)	I_c (-)	I_p (%)
Site 1										
1	1.90	19.62	9.66	0.8	42.9	1.4	26.49			
2	2.10	17.94	1.15					78.27	0.74	20
3	2.30	17.77	0.51					29.54	0.58	30
4	6.70	19.98	11.84	0.6	40.4	0.7	60.42			
5	3.00	20.24	11.89	0.5	39.0	0.6	78.02			
Site 2										
1	2.80	19.91	10.25	0.8	43.0	1.3	30.12			
2	2.00	18.11	0.52					32.05	0.59	40
3	1.20	18.71	3.12	0.4	35.8	0.4	24.06			
4	0.60	18.06	0.69					40.95	0.64	35
5	4.40	20.85	22.74	0.8	43.7	1.0	93.23			
6	4.80	20.16	8.38	0.4	37.3	0.4	68.77			
7	1.20	20.27	14.52	0.5	39.5	0.6	88.63			
Site 3										
1	2.50	18.79	2.63	0.5	38.2	0.5	15.38			
2	3.50	17.09	0.29					15.11	0.47	20
3	1.70	18.12	2.43	0.3	33.9	0.3	19.46			
4	0.60	16.81	0.50					25.30	0.58	25
5	2.60	19.94	10.47	0.6	39.9	0.7	57.16			
6	0.90	18.10	1.75					110.05	0.82	30
7	9.70	20.00	12.73	0.5	39.0	0.6	75.59			
Site 4										
1	1.55	19.55	7.07	0.69	41.98	1.14	23.04			
2	4.45	17.53	0.51					31.20	0.58	30
3	2.80	17.97	5.16	0.32	34.74	0.45	25.26			
4	3.20	20.73	22.54	0.72	42.45	0.89	104.32			
5	5.30	19.02	5.72	0.31	34.24	0.33	49.25			
6	1.00	20.66	26.83	0.63	41.11	0.77	118.80			

$$a_l = \frac{\sqrt{3}(3 - \sin(\varphi_c))}{2\sqrt{2}\sin(\varphi_c)}\,,\ f_e = \left(\frac{e_c}{e}\right)^{\beta},\ f_d = \left(\frac{e - e_d}{e_c - e_d}\right) \quad \text{and} \tag{B5}$$

$$f_b = \frac{h_\mathrm{s}}{n_e}\left(\frac{e_\mathrm{i0}}{e_\mathrm{c0}}\right)^{\beta}\frac{1 + e_i}{e_i}\left(\frac{3p'}{h_\mathrm{s}}\right)^{1-n_e}\left[3 + a_l^2 - a_l\sqrt{3}\left(\frac{e_\mathrm{i0} - e_\mathrm{d0}}{e_\mathrm{c0} - e_\mathrm{d0}}\right)^{\alpha}\right]^{-1}. \tag{B6}$$

For an in-depth explanation of the equations of the hypoplastic constitutive law, refer to the work of von Wolffersdorff [35]. The intergranular strain tensor according to Niemunis [36] is represented by $\hat{\delta}$. The stress rate $\dot{\boldsymbol{\sigma}}$ is calculated from:

$$\dot{\boldsymbol{\sigma}} = \mathsf{E} : \dot{\varepsilon} \tag{B7}$$

where the stiffness tensor E is defined by:

$$\mathsf{E} = [\zeta^{\chi} m_\mathrm{T} + (1 - \zeta^{\chi}) m_\mathrm{R}]\mathsf{L} + \begin{cases} \zeta^{\chi}(1 - m_\mathrm{T})\mathsf{L} : \hat{\delta}\hat{\delta} + \zeta^{\chi}\mathsf{N}\hat{\delta} & \text{for} \quad \hat{\delta} : \dot{\varepsilon} > 0 \\ \zeta^{\chi}(m_\mathrm{R} - m_\mathrm{T})\mathsf{L} : \hat{\delta}\hat{\delta} & \text{for} \quad \hat{\delta} : \dot{\varepsilon} \leq 0 \end{cases} \tag{B8}$$

with the material parameters χ, m_R, m_T and R_max govern the influence of intergranular strain.

$$\zeta = \|\widehat{\delta}\| / R_\mathrm{max}\ . \tag{B9}$$

The evolution equation for the intergranular strain tensor is:

$$\dot{\hat{\delta}} = \begin{cases} (\mathbf{I} - \hat{\delta}\hat{\delta}\zeta^{\beta_\mathrm{R}}) : \dot{\varepsilon} & \text{for} \quad \hat{\delta} : \dot{\varepsilon} > 0 \\ \dot{\varepsilon} & \text{for} \quad \hat{\delta} : \dot{\varepsilon} \leq 0 \end{cases} \tag{B10}$$

where β_R is another material parameter and $\mathbf{I}$ is the fourth-order identity tensor.

Appendix C: Numerical Modelling of CPT-Tests to Validate the Assumed Void Ratios

In order to calibrate the calculated void ratios from the empirical Eq. 4 an axisymmetric FE-model is created to conduct numerical cone penteration

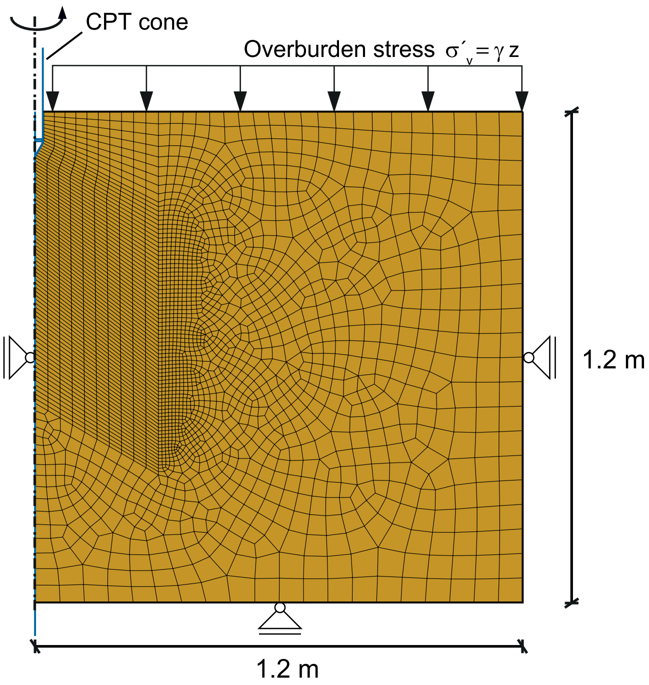

FIGURE C1 | Finite element axisymmetric model for the simulation of the CPT testing.

tests. The so-called zipper method in Abaqus/Standard 2022 with an implicit solver, as depicted in Figure C1, is employed. The zipper method originated from Mabsout [71], consists of soil entity (1×1 m), two rigid bodies representing the cone and a rigid, frictionless tube at 1 mm from the axis of symmetry. The cone slides alongside the tube, displacing the subsoil like a zipper and causing penetration. The cone diameter is set according to [72] to D_{cone} = 35.7 mm and has an aperture angle of 60°. The simulation was conducted with geometric non-linearity and large strain formulation to account for the large strains induced in the elements around the CPT. This option was activated through the non-linear geometry option (NLGEOM) in Abaqus. At the start of the simulation, the cone is pre-inserted into the subsoil to about five times its diameter using the wished-in-place method. The subsoil is modelled with 3462 continuum elements of the type CAX4 using those mentioned above hypoplastic and visco-hypoplastic constitutive parameters in Tables 3 and 4.

The mesh is refined in the region surrounding the cone penetration to capture the local soil behaviour more accurately. The non-cohesive layers are assumed to be saturated and ideally drained during cone penetration with a soil's unit weight γ of 18 kN/m^3 above the groundwater table (GWT), and 11 kN/m^3 below the groundwater table. The soil's unit weight of the cohesive layers is set to γ = 11 kN/m^3 under saturated undrained conditions. A stick-slip model with a low friction coefficient of $\mu = 0.1$ represents the cone's smooth surface. The finite element simulation initiates with a K_0 stress distribution, where the earth pressure coefficient $K_0 = 1 - \sin(\varphi)$, except for peat, where a value of $K_0 = 0.3$ was adopted based on Yamaguchi [42], due to the empirical expression yielding unsatisfactory values compared to laboratory measurements. The representing overburden pressures σ'_{v} are applied as distributed loads on the top of the soil entity. In the first step, gravity is applied to the model. In the second step, the cone is pushed into the soil at a constant velocity of 1 cm/s, corresponding to the velocity of the probing in the field, until a constant tip resistance is reached. Figure C2 shows the resulting tip resistances of the investigated layers. Table C1 compares the observed tip resistances in the field tests with the corresponding numerical simulations, where q_{c} in the field represents the averaged tip resistance of the corresponding layer, obtained from Figure C2, and $q_{\text{c,FEM}}$ in FEA represents the simulated tip resistance. It can be seen that a good agreement between the field measurements and the numerical results exists. Consequently, the selected relative densities are validated for further analysis in the pile load tests.

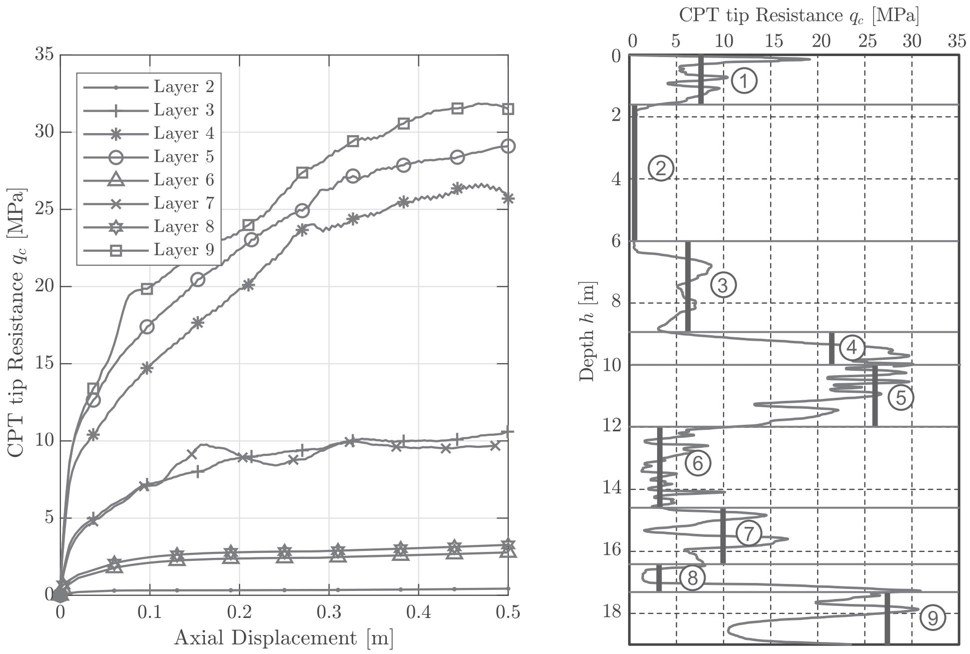

FIGURE C2 | Simulated CPT resistances for the investigated soil layers (left) and measured CPT sounding results along with fitted assumptions represented by vertical bold black lines (right).

TABLE C1 | Overview of assumed void ratios for the soil layers based on comparing CPT results from field explorations and numerical simulations.

	Unit	Layer 2	Layer 3	Layer 4	Layer 5	Layer 6	Layer 7	Layer 8	Layer 9
Soil type	(-)	Peat	Sand II	Sand III	Sand II	Silt	Sand I	Silt	Sand II
Stress σ'_{v}	(kPa)	27.9	76.85	107.65	120.85	150	173.32	191.58	201.15
Void ratio e_0	(-)	2.72	0.6	0.45	0.5	0.51	0.7	0.7	0.55
Rel. density I_{D}	(-)	—	0.66	0.78	0.93	—	0.56	—	0.79
$q_{\mathrm{c,FEM}}$ in FEA	(MPa)	0.35	9.64	24.85	26.56	3.0	9.90	2.9	29.19
q_{c} in field	([MPa)	0.5	8.0	25.0	26.0	2.0	10.0	3.0	28.0